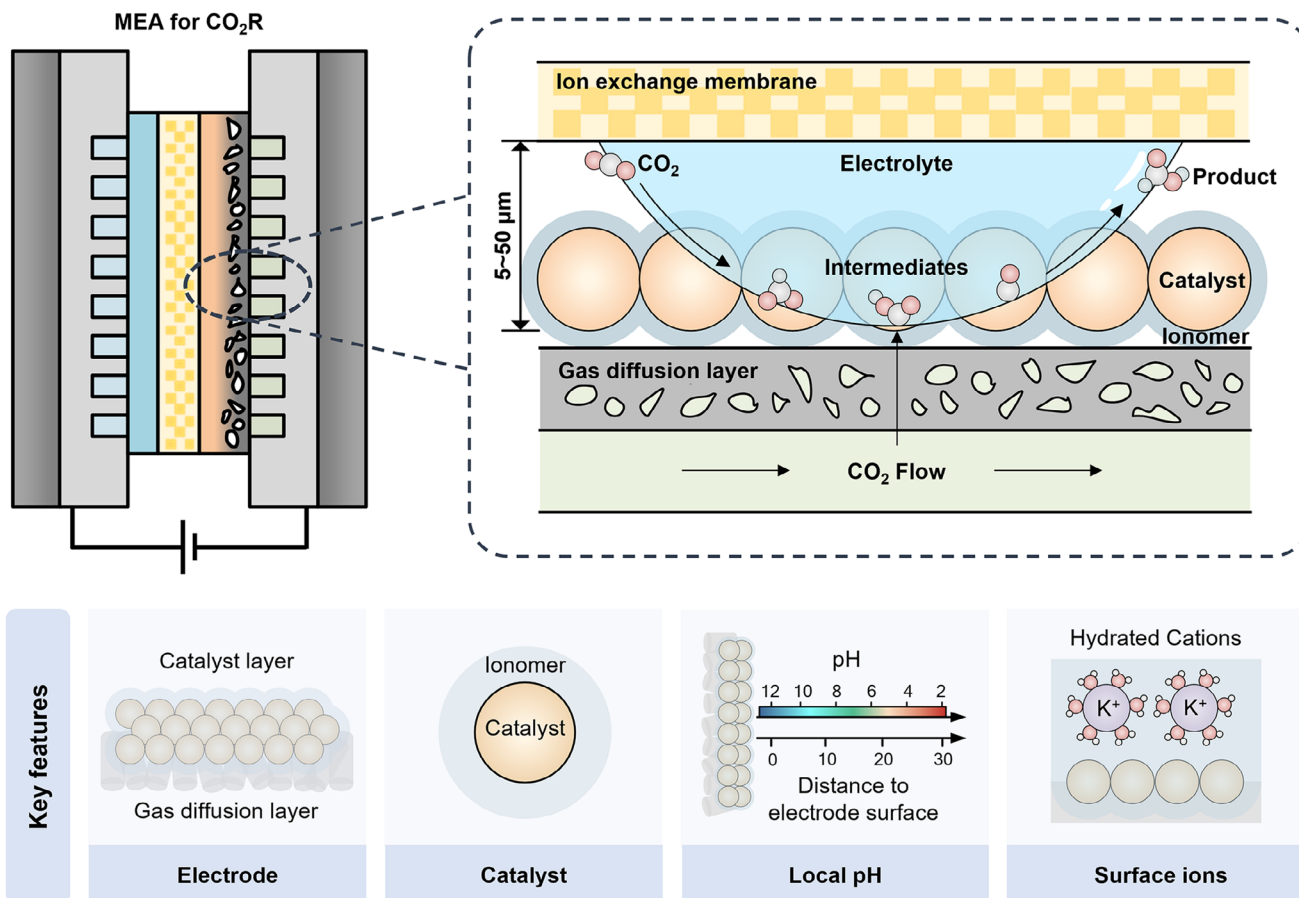


Electrochemical CO₂ Reduction Using Membrane Electrode Assemblies: Progress, Challenges, and Opportunities

Yuhang Jiang^{#, [a]}, Le Li^{#, [a]}, Jin Zhang^{#, [a]}, Weihang Li,^[a] Xiaotong Zhao,^[a] Yi Xie,^[a] Mengyang Guo,^[a] and Miao Zhong^{*[a, b]}



Electrochemical CO₂ reduction (CO₂R) offers a promising route for converting waste CO₂ into valuable short-chain (C₁–C₃) hydrocarbon chemicals using renewable electricity. Substantial progress has been made in elucidating CO₂R reaction mechanisms and in designing high-performance electrocatalysts and electrode structures. Building on these developments, recent efforts have increasingly focused on system-level optimization to fully harness the potential of electrocatalysts for achieving new benchmark efficiencies under practical conditions. Among different CO₂R device configurations, zero-gap membrane electrode assembly (MEA) electrolyzers—typically consisting of catalyst-coated gas diffusion electrodes (GDEs) pressed tightly against an ion-exchange membrane—have shown promise for achieving

high CO₂R current densities at low cell voltages. However, critical challenges remain in the MEA-based CO₂R systems that must be addressed before large-scale deployment. This review discusses recent advances in MEA-based CO₂R, providing cross-scale analyses that connect microscale reaction kinetics, mesoscale mass transport, and device-level integration. It identifies key performance indicators that capture the complex interplay between catalysts, electrode structures, and the overall reaction system, serving as a foundation for the rational design of components and MEA systems toward efficient and scalable operation. With these insights, this review discusses opportunities and challenges for advancing MEA devices toward sustainable and practical CO₂-to-chemical conversion.

1. Introduction

The anthropogenic carbon dioxide (CO₂) emissions resulting from the ever-growing industrial metabolism have significantly influenced the natural carbon cycle established by photosynthesis and the earth's ecosystems.^[1] Achieving global carbon neutrality (net-zero greenhouse gas emissions) poses a formidable challenge—one that demands effective implementation of CO₂ capture, utilization, and storage (CCUS), alongside efficient renewable energy technologies.^[2] According to the recent techno-economic (TEA) report, by 2030, renewable energy sources has the potential of supplying 60% of global electricity demand, providing over 8000 TWh annually through integrated wind, hydro, and solar hybrid power systems.^[1,2] These rapid advancements in renewable electricity generation present great opportunity for electrochemical CO₂ reduction (CO₂R) techniques to convert CO₂ into valuable industrial feedstocks and liquid fuels.

Among various CO₂R devices, the zero-gap membrane electrode assembly (MEA) stands out as one of the most efficient configurations for achieving high CO₂R activity and energy efficiency (EE). The typical MEA electrolyzer consists of a cathode gas diffusion layer (e.g., porous carbon paper or polytetrafluoroethylene (PTFE)), a cathode catalyst layer (e.g., transitional metal catalysts or *p*-block metal catalysts), an ion-exchange membrane (e.g., an anion exchange membrane such as Sustainion from Dioxide Materials, Fumasep from FUMATECH BWT GmbH or a cation exchange membrane such as Nafion from Dupont, GORE-SELECT from W. L. Gore & Associates), and an anode catalyst layer (e.g., Ni foam or IrO₂ catalysts on Titanium

mesh), as shown in Figure 1a. The cathode gas diffusion layer facilitates CO₂ transport while maintaining a high electrical conductivity, together with the catalyst layer above it, this structure forms a triple-phase interface that is crucial for efficient CO₂ transport and reduction. The ion-exchange membrane selectively transports H⁺ or OH[−] ions depending on the reaction environment—acidic, alkaline, or neutral—while preventing the crossover of CO₂R products. On the anode side, the water oxidation (OER) occurs, generating O₂ and completing the overall reaction: CO₂ + H₂O → C_xH_yO_z + O₂. In this cell configuration, the cathode is directly pressed against the ion exchange membrane (Figure 1a,b), creating a compact electrolyzer structure that reduces voltage losses typically associated with the use of aqueous catholytes. Moreover, by leveraging GDEs, the CO₂ transport to the gas–liquid–solid reaction interface is greatly enhanced, allowing CO₂R reaction to proceed at elevated current densities. Under ambient CO₂ feed conditions, the saturated CO₂R current density can reach over 10 A cm^{−2}. However, under these high current density conditions, key challenges arise in achieving high CO₂R selectivity toward a single product while simultaneously maximizing energy efficiency, CO₂ conversion efficiency, and system operational stability.

Efforts have been devoted to improving these performance metrics. Figure 1c,d summarize the state-of-the-art MEA-based CO₂R performance benchmarks at high current densities. For example, formate production has achieved Faradaic efficiencies (FEs) exceeding 90% with *p*-block metal catalysts (such as Bi, Pb, Sn, and their alloys), CO has reached over 95% on weak *CO binding catalysts (such as Ag, Au metals, and Ni single atom catalysts (Ni-SACs)), and, ethylene (C₂H₄) has shown near 80% FE on Cu-based catalysts under optimized conditions. Enhancing CO₂R selectivity to alcohols remains more challenging: ethanol has shown 65% FE using an optimized Cu-2,3,7,8-tetraaminophenazine-1,4,6,9-tetraone (Cu-TAPT) catalyst; Acetate has reached nearly 90% FE with Cu-in-Ag dilute alloy catalysts in pressurized systems; and n-propanol has achieved approximately 47% FE with Cu–Sn catalysts. It should be noted that some of these values remain insufficient for practical application. More critically, energy efficiency, a key performance metric tied to commercial viability, needs to be further improved. The highest reported full-cell energy efficiencies in MEA based

[a] Y. Jiang[#], L. Li[#], J. Zhang[#], W. Li, X. Zhao, Y. Xie, M. Guo, M. Zhong
College of Engineering and Applied Sciences, Nanjing University, Nanjing 210023, China
E-mail: miaozhong@nju.edu.cn

[b] M. Zhong
Collaborative Innovation Centre of Advanced Microstructures, National Laboratory of Solid State Microstructures, Frontiers Science Center for Critical Earth Material Cycling, College of Engineering and Applied Science, Nanjing210023, China

[#] These authors contributed equally to the manuscript as co-first authors.

systems are 60% for formate, and 45% for CO and 41% for C₂H₄, which approach the minimum requirements of 60% FEs for CO and formate, and 40% FE for C₂H₄ projected by TEA, with the consideration of product market prices and industrial electricity costs. This energy efficiency shortfall primarily arises

from slow reaction kinetics at catalyst surface and partial energy losses during mass and charge transport across the electrode and electrolyte. Moreover, achieving long-term CO₂R stability remains an unsolved challenge. Commercial electrolysis requires continuous operation over 10,000 h with <5% performance



Mr. Yuhang Jiang received his master's degree in materials science and engineering from East China University of Science and Technology in 2024. He is a PhD candidate in the College of Engineering and Applied Sciences, Nanjing University, where his research focuses on the design of electrocatalysts for electrochemical CO₂ and CO reduction.



Miss Xiaotong Zhao has obtained a master's degree from the College of Engineering and Applied Sciences of Nanjing University. Her main research focused on electrochemical reduction of CO₂.



Dr. Le Li received her PhD degree at the College of Engineering and Applied Sciences, Nanjing University in 2024. She continued her research as a postdoctoral fellow at Nanjing University, focusing on the electrochemical reduction of CO₂ in membrane electrode assemblies and related applications.



Miss Yi Xie has obtained a master's degree from the College of Engineering and Applied Sciences of Nanjing University, during which time her research focused on photothermal catalytic reactions.



Dr. Jin Zhang is currently a postdoctoral fellow at Nanjing university. He received his PhD degree (2023) from Nanjing university. His research interests are novel catalysts synthesis for energy storage and catalysis.



Mr. Mengyang Guo is now a PhD candidate at Nanjing University, China. His research mainly focuses on electrocatalysis and CO₂ utilization.



Mr. Weihang Li is currently a PhD student at the College of Engineering and Applied Sciences, Nanjing University. His primary research focuses on the electrochemical C–N coupling and related applications.



Dr. Miao Zhong is a professor at Nanjing University, China. He received his PhD from School of Engineering, the University of Tokyo, Japan. He then worked as a JSPS postdoctoral fellow and a project senior researcher for the Artificial Photosynthetic Project of NEDO at the University of Tokyo. Later he worked as a postdoctoral fellow at University of Toronto, Canada. His current research focuses on catalysis, energy conversion, and related applications.

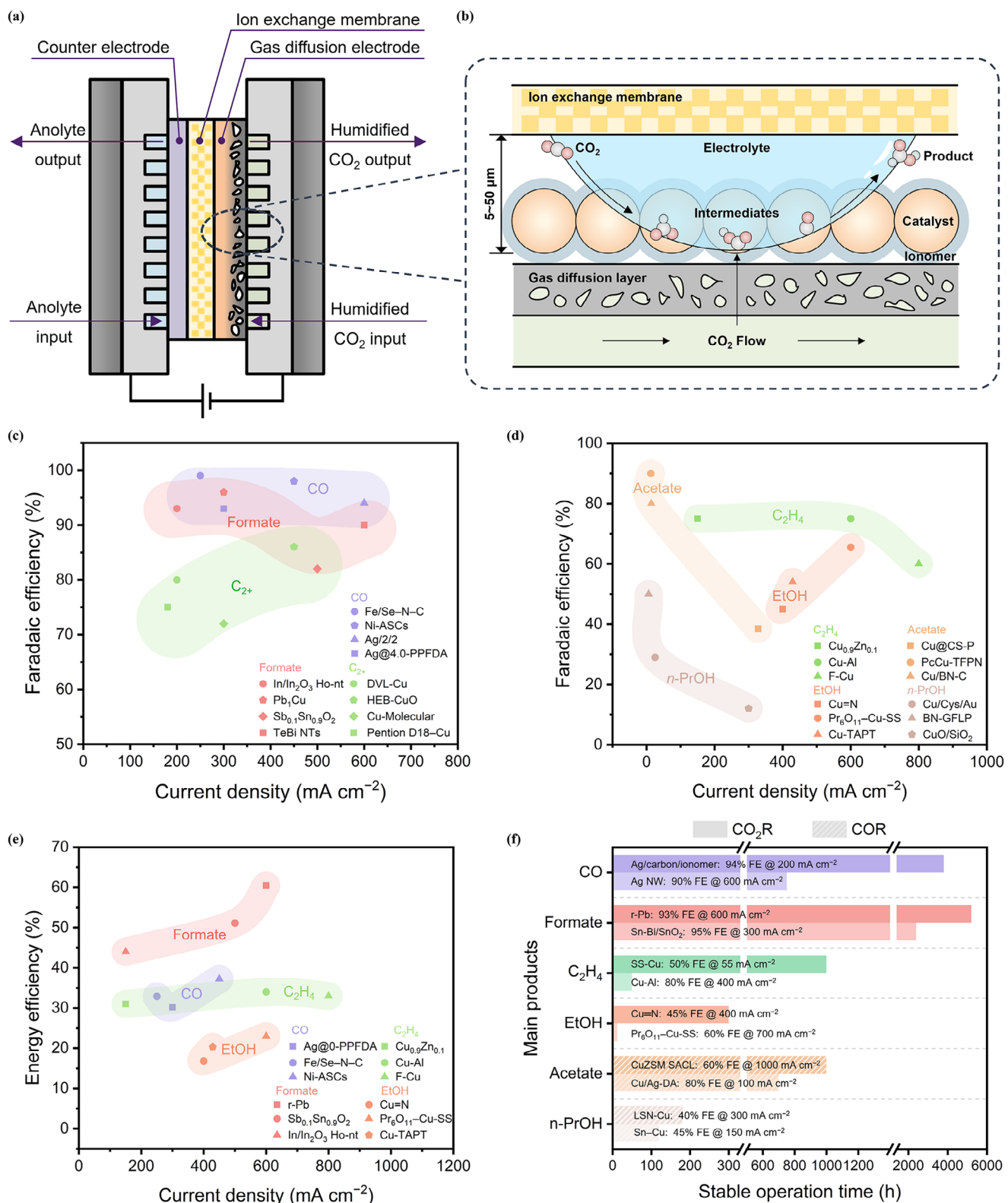


Figure 1. (a) A schematic illustrating the membrane electrode assembly (MEA) structure. (b) A 1D schematic illustrating the three-phase reaction on a gas diffusion electrode (GDE), which consists of a gas diffusion layer (GDL), a partially wet catalyst layer (CL), and a top electrolyte layer. (c–f) Performance of CO₂ electroreduction in the reported MEA systems: (c, d) Faradaic efficiencies (FEs) for CO₂ electroreduction to C₁–C₂₊ products, (e) the full-cell energy efficiencies, and (f) the stability across a range of current densities.

degradation, yet few CO_2R catalysts, especially those based on easily reconstructed Cu catalysts, have met this standard.^[3] Stability issues also persist at the membrane and electrode, showing the urgent need to develop a durable system.

In this review, we discussed the recent advancements in electrochemical CO_2R technologies, following the sequences from catalysts to electrodes and membranes, and finally to the electrochemical systems. We highlight that kinetics and intermediate binding energetics are primarily catalyst-driven, whereas mass and charge transport are closely tied to electrode and membrane design. Addressing these fundamental microscale aspects is essential to enable system-level advances in CO_2R accessibility and conversion efficiency. Finally, we analyze the challenges associated with the long-term stability and scaling-up of the current devices. We expect, through continuous innovation and development, MEA-based electrolyzers to advance toward sustainable CO_2 conversion and the efficient production of valuable chemical products.

2. Catalyst and Electrode for Electrochemical CO_2R

In membrane electrode assembly (MEA) electrolyzer (Figure 1b), the cathode—comprising catalyst materials coated on a porous, electrically conductive gas diffusion layer (GDL)—is pressed on an ion-exchange membrane. This configuration facilitates CO_2 diffusion through the GDL and water transport from the membrane, creating a three-phase interface at the catalyst layer. A 0.5–20 μm thin catalyst layer is therefore crucial for enhancing mass and charge transport in the CO_2R reaction. When transport limitations are minimized, catalyst properties become the primary factor determining MEA electrolyzer performance. Table 1 summarizes the leading catalysts currently enabling state-of-the-art production of CO, formate, and C_{2+} products, along with their corresponding operating conditions that shape local reaction environment and impact overall efficiency. Table 2 summarizes the competing reactions during CO_2R and the reported approaches to address them. In this section, we examine how catalyst composition, structure, and local environment collectively influence MEA performance in CO_2 electroreduction.

2.1. Catalysts for CO_2 -to- C_1 Products

2.1.1. Formate

CO_2R reaction to CO and formate involves a simple two-electron transfer process and is currently considered the most economically viable pathway, as it is least sensitive to electricity costs according to TEA. MEA-based electrolyzers have achieved high current densities (hundreds of mA cm^{-2}) and Faradaic efficiencies over 95%. Current research efforts are primarily focused on improving overall energy efficiency and long-term operational stability, alongside scaling up electrolyzers to larger areas ($1,000\text{--}10,000 \text{ cm}^2$) for evaluate the feasibility of industrial applications.

The CO_2R to formate conversion typically involves the crucial ${}^*\text{OCHO}$ intermediate, where the two O atoms are bonded to the catalyst surfaces.^[4] The *p*-block metals (such as Sn, Bi, In, Ga, Pb, and Sb) exhibit suitable O affinity to stabilize the metal–oxygen (M–O) binding.^[5,6] Among these metals, Sn has been shown to exhibit near-optimal ${}^*\text{OCHO}$ binding, facilitating efficient formate conversion. For example, Zhang et al. demonstrated that SnO_2 /graphene composites achieved 78% FE for formate production at 0.68 V overpotentials and a current density of 21.3 mA cm^{-2} .^[7] Hou et al. designed a SnO_2 nanosheet with simultaneous N dopants and oxygen vacancies (denoted as V_O rich N-SnO_2 NS), which achieved 83% FE at $-0.9 \text{ V}_\text{RHE}$. Theoretical calculations revealed that the reaction free energy for ${}^*\text{OCHO}$ protonation was decreased and hydrogen evolution reaction (HER) was suppressed, thus enhancing formate selectivity.^[8] *p*-block metals such as Bi and Pb have been proven to be efficient in stabilizing ${}^*\text{OCHO}$ intermediates and suppressing competing hydrogen evolution, thereby enabling high selectivity toward formate production in CO_2 electroreduction.

Besides *p*-block metals, Cu is another widely used catalyst in CO_2R to formate conversion. In conventional H cell devices, Cu has low selectivity for formate indicating that C–H bond formation occurs to form ${}^*\text{OCHO}$ intermediate on its surfaces at negative potentials. Recently, it showed that alloying Cu with *p*-block metals can significantly enhance selectivity toward formate. Wang et al. showed that the structural reconstruction of CuO/SnO_2 under electrochemical potentials created Cu/SnO_{2-x} heterostructures to achieve 54.8% formate FE and 39.8% ethanol FE, respectively.^[9] Li and Zhong et al. prepared Cu_6Sn_5 on polytetrafluoroethylene (PTFE)-based GDE electrode characterized by strong ${}^*\text{OCHO}$ affinity and weak ${}^*\text{H}$ binding with high selectivity for formate production, achieving over 90% FE formate across a broad current density range from 0.4 to 1.2 A cm^{-2} .^[10] Zeng et al. employed simulation calculations to screen the activity trends of Cu-based bimetallic catalyst and subsequently synthesized a single-atom Pb-alloyed Cu (Pb_1Cu) catalyst (Figure 2a). This catalyst converts CO_2 to formate with a high FE of $\sim 96\%$ with high activity at current densities exceeding 1 A cm^{-2} (Figure 2b). A comparison of the free energy barriers showed that the activated Cu sites in Pb_1Cu regulate the protonation step of CO_2R , favoring the ${}^*\text{OCHO}$ pathway for formate production while suppressing the formation of other products.^[11]

Achieving high formate selectivity and current density is no longer a major challenge; the current focus has shifted to realizing high energy efficiency—especially high stability—while maintaining high selectivity and large current density. Zhong and Li et al. synthesized a uniformly $\text{Bi}_{0.1}\text{Sn}$ catalyst featuring stable Sn-Bi/SnO_2 active surfaces (Figure 2c). This catalyst achieved a formate FE of over 95% and a cathodic EE exceeding 70% at 100 mA cm^{-2} . Additionally, it demonstrated remarkable stability, with CO_2 -to-formate conversion lasting more than 2400 h (100 days) in a flow cell (Figure 2d). Furthermore, the catalyst enabled the stable production of 3.4 moles of concentrated formate over 100 h in a cation-exchange membrane (CEM)-based MEA system.^[12] Recently, Guo et al. developed a series of turing-structured Sb–Sn electrocatalysts, which enable the modulation

Table 1. Recent reports on catalysts for electrochemical CO₂R.

No.	Catalyst	Current Density (mA cm ⁻²)	Main Products	FE (%)	Stability	Refs.	
						Time (h)	Current Density (mA cm ⁻²)
1	Pb ₁ Cu	300	Formate	96	180	100	[11]
2	Sn-Bi/SnO ₂	120	Formate	98	2400	100	[12]
3	Sb _{0.1} Sn _{0.9} O ₂	500	Formate	82	200	500	[13]
4	r-Pb	600	Formate	93	5200	600	[14]
5	2D-Bi	100	Formate	>90	100	100	[15]
6	Fe/Se—N—C	250	CO	99	95	250	[20]
7	Ni-ASCs/4.3 wt.%	450	CO	98	10	360	[25]
8	Ag/carbon/ionomer	600	CO	94	3800	200	[26]
9	Ag-QAPPT	60	CO	80	50	60	[27]
10	Ag@4.0-PPFDA	300	CO	93	100	300	[124]
11	DVL-Cu	200	C ₂ H ₄	80	55	150	[41]
12	Cu-arylpyridiniums	≈300	C ₂ H ₄	72	190	≈300	[47]
13	de-alloyed Cu-Al	600	C ₂ H ₄	80	100	400	[34]
14	Cu _{0.9} Zn _{0.1}	150	C ₂ H ₄	75	150	150	[35]
15	Cu/PFSA	1000	C ₂ H ₄	25	150	150	[77]
16	Cu-QAPEEK	1000	C ₂ H ₄	50	5	200	[91]
17	surface-step-rich Cu	300	C ₂ H ₄	43	1000	300	[92]
18	3D CTPI-Cu	300	C ₂ H ₄	67	220	100	[100]
19	Cu ₂ O cube	≈400	C ₂ H ₄	54	1.5	≈400	[36]
20	F—Cu	1600	C ₂ H ₄	80	N.A.		[43]
21	HEB-CuO NPs	450	C ₂ H ₄	86	50	200	[44]
22	Pention D18-Cu	180	C ₂ H ₄	75	N.A.		[104]
23	Cu=N	400	EtOH	45	300	400	[63]
24	Cu-TAPT	429	EtOH	54	40	≈400	[65]
25	dCu ₂ O/Ag _{2.3%}	800	EtOH	40	12	800	[66]
26	Fe-TPP/Ni	30	EtOH	68	60	5	[68]
27	PcCu-TFPN	12.5	Acetate	90	80	10	[53]
28	Cu@CS-P	328	Acetate	39	30	≈460	[54]
29	Ag _{1%} —Cu ₂ O	200	Acetate (COR)	70	18	100	[55]
30	Cu/Ag DA	≈125	Acetate (COR)	91	820	100	[56]
31	CuPd	607	Acetate (COR)	70	500	500	[57]
32	CuZSM SACL	1000	Acetate (COR)	71	1000	1000	[60]
33	CuO/3DOM SiO ₂	300	n-PrOH	12	120	100	[72]
34	Cu/Cys/Au	25	n-PrOH	29	10	25	[74]
35	Sn—Cu	150	n-PrOH (COR)	47	120	150	[75]

of interfacial water reorientation by tuning surface oxophilicity (Figure 2e). The best-performing Sb_{0.1}Sn_{0.9}O₂ achieved a formate FE of 92.0% at 1000 mA cm⁻² and operated stably for 200 h at 500 mA cm⁻² in a MEA electrolyzer (Figure 2f).^[13]

To prevent the formation of carbonate, an acidic electrolyte was employed for the electrochemical reduction of CO₂. Xia et al. developed a proton exchange membrane (PEM) system (Figure 2g) that utilizes a recycled Pb (r-Pb) catalyst to achieve FE exceeding 93% for formic acid. Through the start-up/shut-down processes (during this process, the GDE is reprocessed

every 200 h using a PTFE emulsion to maintain the stability of the three-phase interface), the catalyst achieved a single-pass CO₂ conversion efficiency of nearly 91% at a current density of 600 cm⁻² and a cell voltage of 2.2 V, and demonstrated stable performance over more than 5400 h of operation (Figure 2h).^[14]

Utilizing a solid-state electrolyte (SSE) reactor presents a promising pathway for selectively separating pure liquid products such as formic acid, acetic acid, and alcohols. Typically, an SSE, such as a proton-conducting polymer, is placed between the anion-exchange membrane (AEM) and CEM in close prox-

Table 2. A short summary of the competing reactions during CO₂R and the approaches to address them.

Target Products	Competing Reaction	Characteristics of the Competing Reaction	Approaches to Address the Competing Reactions
Formate (Thermodynamic potential: -0.199 V _{RHE}) CO (Thermodynamic potential: -0.1 V _{RHE})	HER (Thermodynamic potential: 0 V _{RHE})	1. Favorable on Pd, Pt, Ni, and reconstructed Cu-based catalysts with moderate-H binding, etc. 2. Strong in an acidic environment.	1. Develop catalysts with enhanced CO ₂ R kinetics over HER: For formate production: develop active p-block metal (Bi, Sn, Pb, etc.) and bimetallic (Cu-Bi, Cu-Sn, etc.) catalysts ^[9,10] to increase the coverage of *OCHO intermediates ^[5,6] For CO production: Design transition metal catalysts with weak *CO bonding (e.g., Au, Ag, Fe _x /Au etc.) to enhance CO ₂ protonation kinetics and facilitate rapid *CO desorption ^[22,23] . 2. Suppress HER by increasing its energy barriers. 3. Increase surface cation concentrations (such as K ⁺ , Rb ⁺ , Cs ⁺) to promote CO ₂ R while simultaneously suppressing HER. 4. Elevate local pH at the reaction interface to favor CO ₂ R over HER. 5. Apply hydrophobic surface coatings to increase CO ₂ concentrations at the electrode surface ^[101-104] .
C ₂ ⁺ (Thermodynamic potential: 0.06 V _{RHE} for ethylene, 0.09 V _{RHE} for ethanol)	CO production (Thermodynamic potential: -0.1 V _{RHE}); formate production (Thermodynamic potential: -0.199 V _{RHE}); HER (Thermodynamic potential: 0 V _{RHE})	For CO formation: ·Favorable on Ag, Zn, Au-based catalysts with weak CO binding For formate formation: ·Favorable on Sn, Bi, In-based catalysts with strong O binding For HER: ·Favorable on Pd, Pt, Ni, and reconstructed Cu-based catalysts with moderate-H binding, etc.	1. Develop active Cu-based catalysts with optimal *CO binding—neither too strong nor too weak—through strategies such as surface facet engineering ^[37,38] . 2. Induce asymmetric *CO adsorption on heteroatom active sites (e.g., Cu-Al, Cu-Ag) ^[34,35,35,67,41,42,65] to facilitate C-C coupling. 3. Dope halogen elements into Cu or create Cu ⁺ -Cu interfaces to modulate charge density on Cu to promote C-C coupling. 4. Functionalize the Cu surface with organic molecules or hydrophobic coatings to increase local CO ₂ coverage ^[101-104] . 5. Enhance cation and anion effects (e.g., using high concentrations of K ⁺) ^[77,84] to promote C-C coupling. 6. Increase local pH (e.g., via surface ionomer coatings) ^[82] to promote C-C coupling while suppressing HER.

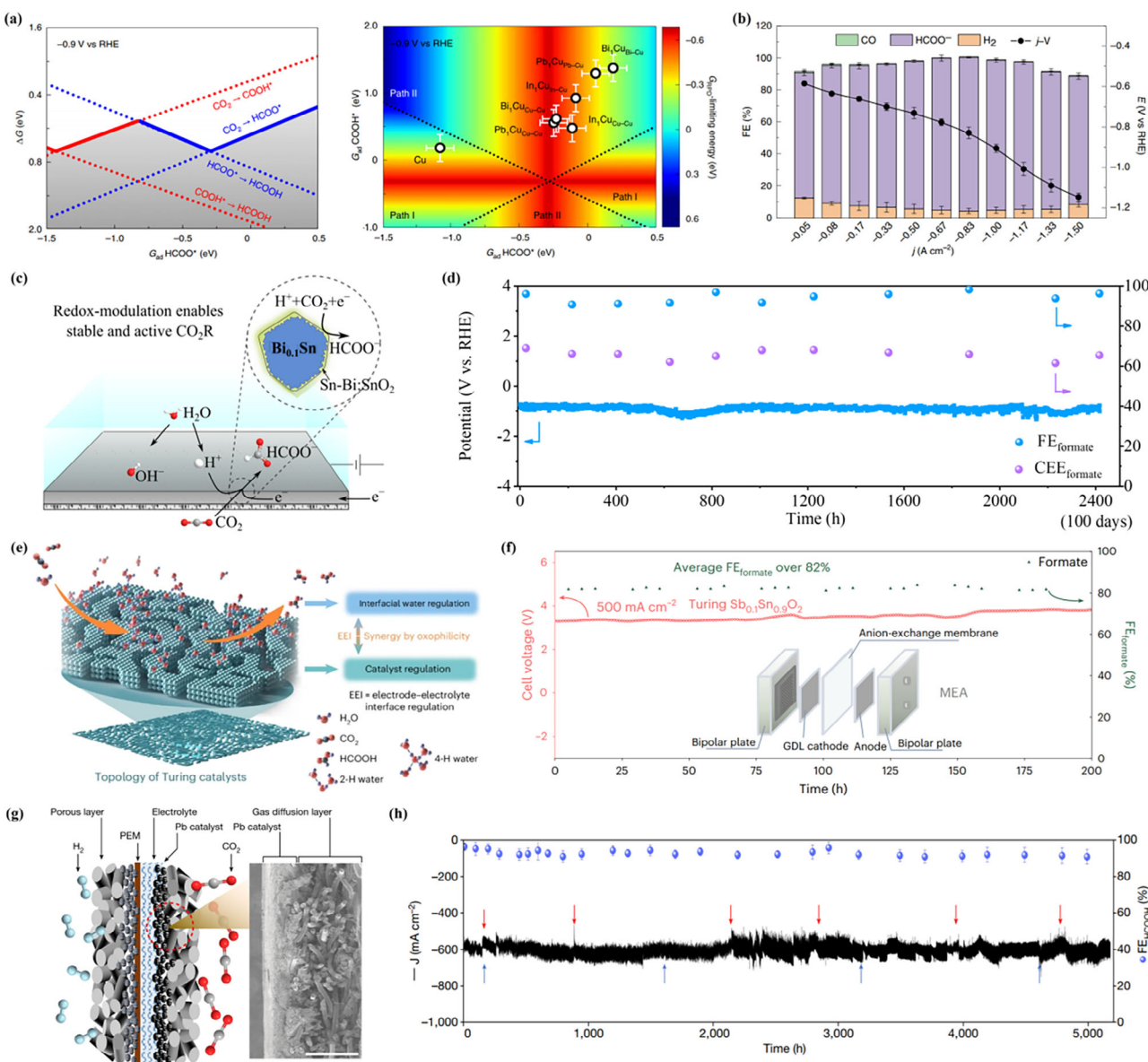


Figure 2. (a) (Left) 1D reaction phase diagram (RPD) for CO₂R showing the free energy profiles of key steps via COOH (red) and HCOO* (blue) pathways. (Right) 2D RPD for formate production, based on adsorption free energies of HCOO* and COOH* on different surfaces. (b) FEs of all CO₂R products at different current densities and the corresponding *j*-V curve of Pb₁Cu SAAs.^[11] Copyright 2021, Springer Nature. (c) Schematic of a redox-modulated Bi_{0.1}Sn/SnO₂ surface on Bi_{0.1}Sn during the electrochemical reaction. (d) CO₂R performance in a flow-cell system: Chronopotentiometry (blue line), FE (blue dots), and half-cell energy conversion efficiency (purple dots) for formate production in 1 M KHCO₃ and KOH at 100 mA cm⁻².^[12] Copyright 2021, Springer Nature. (e) Schematic illustration of the topological structure of the Turing Sb_{0.1}Sn_{0.9}O₂ catalyst, tuning surface oxophilicity to reorient interfacial water and promote CO₂-to-formate conversion. (f) Durability test (red line) and corresponding FE_{formate} (green dots) of continuous 200 h electrolysis in a 5-cm² MEA electrolyzer at 500 mA cm⁻². Inset: schematic illustration of the MEA configuration.^[13] Copyright 2025, Springer Nature. (g) Schematic diagram of a PEM electrolyser used for CO₂R. Right: cross-sectional SEM image of a fabricated cathode electrode. (h) Electrochemical stability of the PEM reactor at a cell voltage of 2.2 V. Positions indicated by red and blue arrows represent those of replacement of electrolyte and reaction gas, respectively.^[14] Copyright 2024, Springer Nature.

imity (Figure 3a). Notably, significant progress has been made in using SSEs to produce pure, electrolyte-free formic acid in CO₂R systems. Wang et al. reports high-purity 12.1 M HCOOH solution through electrocatalytic CO₂R using SSEs, with stable production of ~0.1 M HCOOH for over 100 h (Figure 3b).^[15] Building on this, Wang et al. further developed an all-solid-state CO₂R reactor featuring a porous solid electrolyte (PSE) layer that separates the cathode and anode (Figure 3c). Formate ions and

protons recombine within the PSE to form formic acid, which is then extracted in vapor form by an inert gas stream. By using a Bi catalyst enriched with grain boundaries, the system achieved ~450 mA cm⁻² formate partial current density at a ~97% FE, and enabled the production of 100 wt.% formic acid solutions through vapor condensation (Figure 3d).^[16] Li and Zhong et al. prepared Cu₆Sn₅ with strong *OCHO affinity and weak *H binding on PTFE-based GDE. This electrode produced

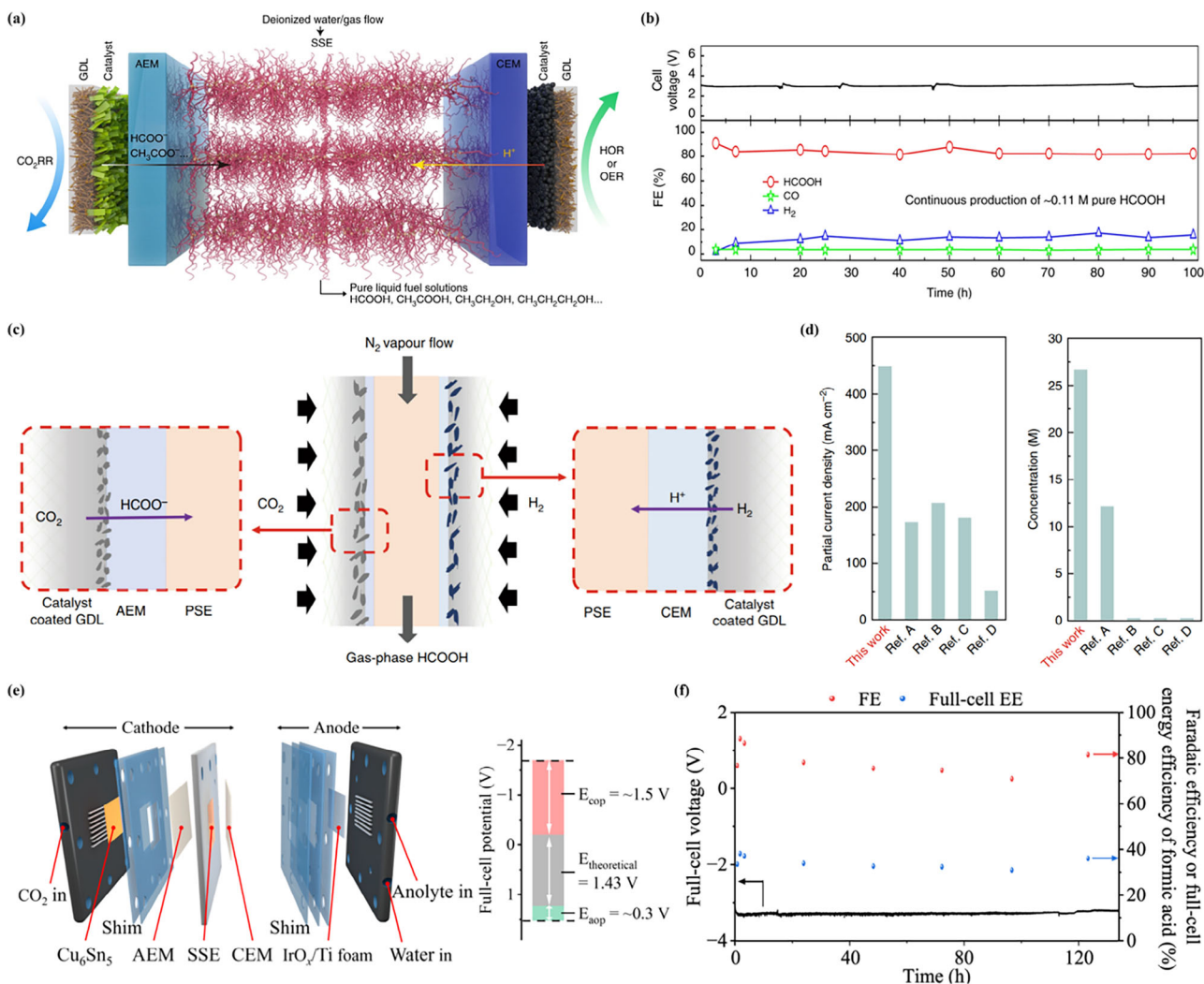


Figure 3. (a) Schematic of the CO_2 reduction cell with a solid electrolyte (SSE) that can conduct either anions or cations. (b) Long-term stability test showing consistent high selectivity of HCOOH production with the 2D-Bi catalyst at 30 mA cm^{-2} over 100 h.^[15] Copyright 2019, Springer Nature. (c) Schematic of CO_2 reduction to formic acid in an all-solid-state reactor, with HCOO^- and H^+ ions recombining in the PSE and released as vapor by N_2 flow. (d) The electrochemical performance of all-solid-state CO_2R reactor compared with previous literature (A: ref. [15], B: ref. [17], C: ref. [18], D: ref. [19]).^[16] Copyright 2020, Springer Nature. (e) Structure of a solid-state-electrolyte-based membrane electrode assembly electrolyzer for CO_2R and its potential distribution. (f) FEs and full-cell energy efficiencies of formic acid production with Cu_6Sn_5 at 100 mA cm^{-2} during 130-h CO_2R operation. Copyright 2024, Springer Nature.

0.36 M pure formic acid with 88% FE and 37% full-cell EE over 130 h in an SSE-based MEA electrolyzer (Figure 3e,f).^[10]

2.1.2. CO

In electrochemical CO_2R -to-CO conversion, metals with weak CO binding, such as Au and Ag, are commonly used. The weak binding of CO allows for its desorption from the catalyst surfaces prior to further *CO hydrogenation to form hydrocarbons or C–C coupling to form C_{2+} products. In such cases, the energy-limiting step is the protonation CO_2 to *COOH ($\text{CO}_2 + \text{H}^+ + \text{e}^- \rightarrow *{\text{COOH}}$).^[20,21] To lower the energy barrier in this step, Kanan et al. reported that an oxide-derived Au catalyst exhibited >96.3% CO FE at an overpotential of 240 mV, which is primarily attributed to the stabilization of $\text{CO}_2^{\delta-}$ on the oxide-derived Au surfaces.^[22] Yao et al. designed a bimetallic catalyst composed of atomically

dispersed Fe on Au nanoparticles (Fe_1/Au) exhibiting a CO_2 -to-CO FE of up to 96% at $-0.65 \text{ V}_{\text{RHE}}$. They suggested that synergistic interaction between the Fe single atoms and the nearby Au facilitated the adsorption/activation of CO_2 , leading to the generation of abundant *COOH species on the Fe_1/Au catalysts for the subsequent reaction.^[23] Ag nanoparticles have also been studied due to their unique advantages of high surface areas. Jiao et al. reported a nanoporous Ag catalyst for more effectively stabilizing CO_2^- intermediates on the highly curved surface, which is capable of reducing CO_2 to CO at moderate overpotentials of <0.50 V, with a CO selectivity up to 92%.^[24]

Similar to the progress of formate production, high selectivity has been achieved to produce CO.^[25] Efforts have been made to improve the long-term stability of CO_2R -to-CO production while maintaining high FE and EE, such as coating catalyst surfaces

with functional organics or ionomers to regulate the three-phase boundary of catalysts. Masel et al. used Sustainion imidazolium-functionalized membranes and ionomers to improve the performance of the CO₂ electrolysis process and found that at a fixed current of 200 mA cm⁻² and an applied potential of about 3 V, 98% CO selectivity was maintained for nearly 4,000 h. They further indicated that it is crucial to keep membrane hydrated continuously for the cell to run for 4,000 h or longer, which is achieved by circulating a 10 mM KHCO₃ solution in anode. Cation (K⁺) transported with water from anode to cathode and anions (OH⁻, HCO³⁻, and CO₃²⁻) carried water from cathode to anode, maintaining water balance in the membrane and prevent dehydration.^[26]

Despite this progress, most processes so far have been made in neutral or alkaline electrolytes, where carbonate precipitation undermines CO₂ utilization efficiency. Recently, Wang et al. tackled this carbonate precipitation challenge by operating under acidic conditions. Their approach achieved a CO partial current density of 105 mA cm⁻² at 4 V, with 80% CO FE, 90% single-pass conversion efficiency, and stable 50 h operation.^[27] This acid-fed system mitigates carbonate formation but requires improvement on the overall CO₂-to-CO conversion energy efficient toward industrial-scale CO₂ to CO conversion.

2.2. Catalysts for CO₂-to-C₂₊ Products

Compared to C₁ products, C₂₊ chemicals such as C₂H₄ and ethanol (C₂H₅OH) and propanol (C₃H₇O) possess significantly larger global markets (C₂H₄: 182 \$billion, C₂H₅OH: 77 \$billion, C₃H₇O: 2.8 \$billion).^[28,29] With the continuous decrease in renewable electricity costs—thereby reducing the levelized cost of CO₂ electroreduction—the electrified production of C₂₊ chemicals has gained increasing research interest.^[30]

To date, Cu remains the most promising catalyst for room-temperature CO₂ electrolysis toward C₂₊ hydrocarbon and oxy-genes. According to the adsorption-activity volcano scaling relations, the *CO binding energy on catalyst is a key descriptor for C–C coupling activity.^[31] Density functional theory (DFT) calculations show that the Cu (211) facet exhibits a moderate *CO binding energy close to -0.67 eV, placing it near the optimal region for electrochemical C–C coupling.^[31] In contrast, metals like Ni and Ru bind *CO too strongly, favoring deep hydrogenation to CH₄, while metals like Ag and Au bind *CO too weakly, causing CO desorption before C–C coupling. These insights explain the moderate-to-high CO₂ to C₂₊ FE with Cu catalyst, however, achieving Faradaic efficiency (FE) > 90% on pure Cu remains a grand challenge. Moreover, EE (>50%) and operational stability (>1,000 h) remain major hurdles for practical deployment of CO₂R technology.

2.2.1. Ethylene

In the early stage of C₂H₄-oriented research, Sargent et al. designed a catalytic electrode that differed from conventional carbon-based GDEs. Specifically, they separated PTFE and carbon nanoparticles (NPs) into distinct layers, with the Cu catalyst sand-

wiched in between (Figure 4a), thereby maintaining an abrupt interface. Compared to the traditional GDE, the graphite/carbon NPs/Cu/PTFE electrode exhibited a stable ethylene FE of ~70% at a constant applied voltage of -0.55 V vs. RHE in 7 M KOH, maintaining continuous operation for over 150 h (Figure 4b).^[32]

To enhance the FE of CO₂R toward C₂₊ products, various strategies—such as alloying, facet engineering, and doping with oxides, halides, or nitrogen—have been explored. Alloying offers a strategy to both modulating local electronic environment of Cu for favorable *CO binding and stabilizing active Cu structures.^[33] To identify such alloy systems, Zhong, Tran, Ulissi, and Sargent employed machine learning integrated with DFT to explore Cu-based bimetallic alloys, identifying Cu–Al alloys (5–15% Al) that achieved >80% C₂H₄ FE at high current densities (400–600 mA cm⁻²) under alkaline conditions (Figure 4d,e).^[34] Later, Zhang and Zhong et al. found that alloying Cu with Zn (5–10% Zn concentration) can improve the C₂₊ FE to 91%, where C₂H₄ FE reaches 73%, and enabled stable operation for over 150 h at 150 mA cm⁻². These enhancements stemmed from introducing a controlled amount of secondary elements with weak CO binding (e.g., Al, Zn, Ag) creates asymmetric *CO adsorption which can lower C–C coupling barriers (Figure 4g).^[35]

As part of facet engineering, DFT studies indicate that Cu(100) and Cu(211) step surfaces exhibit lower C–C coupling barrier.^[36] Sargent et al. demonstrated that enriching Cu (100) facets via electrodeposition significantly enhanced C₂₊ products formation, achieving ~90% FE at a current density of 520 mA cm⁻² due to enhanced intermediate adsorption and lowered surface energy.^[37] Similarly, Huang et al. reported a stable Cu (511) planar [3 (100) × (111)] stepped surface with high FE of 70% towards C₂H₄, maintaining stability for over 200 h. DFT results reveal that Cu(511) provides thermodynamically favorable C₂ pathway, a reduced C₁ pathway barrier, and suppressed HER.^[38]

In addition to facet engineering, modulation of the chemical state of Cu has proven to be effective in enhancing C₂₊ product selectivity. Oxide-derived Cu (OD-Cu), typically prepared via thermal oxidation or anodic treatment, features abundant Cu^{δ+} sites and grain boundaries that modulate the adsorption behavior of key intermediates toward C–C coupling.^[31] Crumlin et al. highlighted that a thin subsurface oxide layer is critical for CO₂ activation in the presence of water, enabling enhanced reactivity.^[39] To rationalize the persistence of Cu^{δ+} species under reductive conditions, Cui et al. proposed a “seesaw effect”, wherein hydroxyl radicals (OH[·]), generated through rapid oxygen exchange between HCO₃⁻ and H₂O, can reoxidize the Cu surface, maintaining a dynamic Cu oxidation state.^[40] Building upon this mechanistic insight, Gong et al. demonstrated that tuning Cu/Cu₂O interfaces to enhance *OCCOH intermediate stabilization led to a high ethylene FE of 84.5% and a full-cell EE of 27.6% at 200 mA cm⁻² in an MEA.^[41] Similarly, Cuenya et al. observed that a dynamic equilibrium between Cu^{δ+} and Cu⁰ species significantly promotes ethanol production, underscoring the importance of maintaining mixed-valence states for enhanced C₂₊ formation.^[42]

Beyond oxides, doping strategies involving halogens, nitrogen, and surface modification strategies involving molecular additive coatings have also shown great promise.^[43–45] Ma

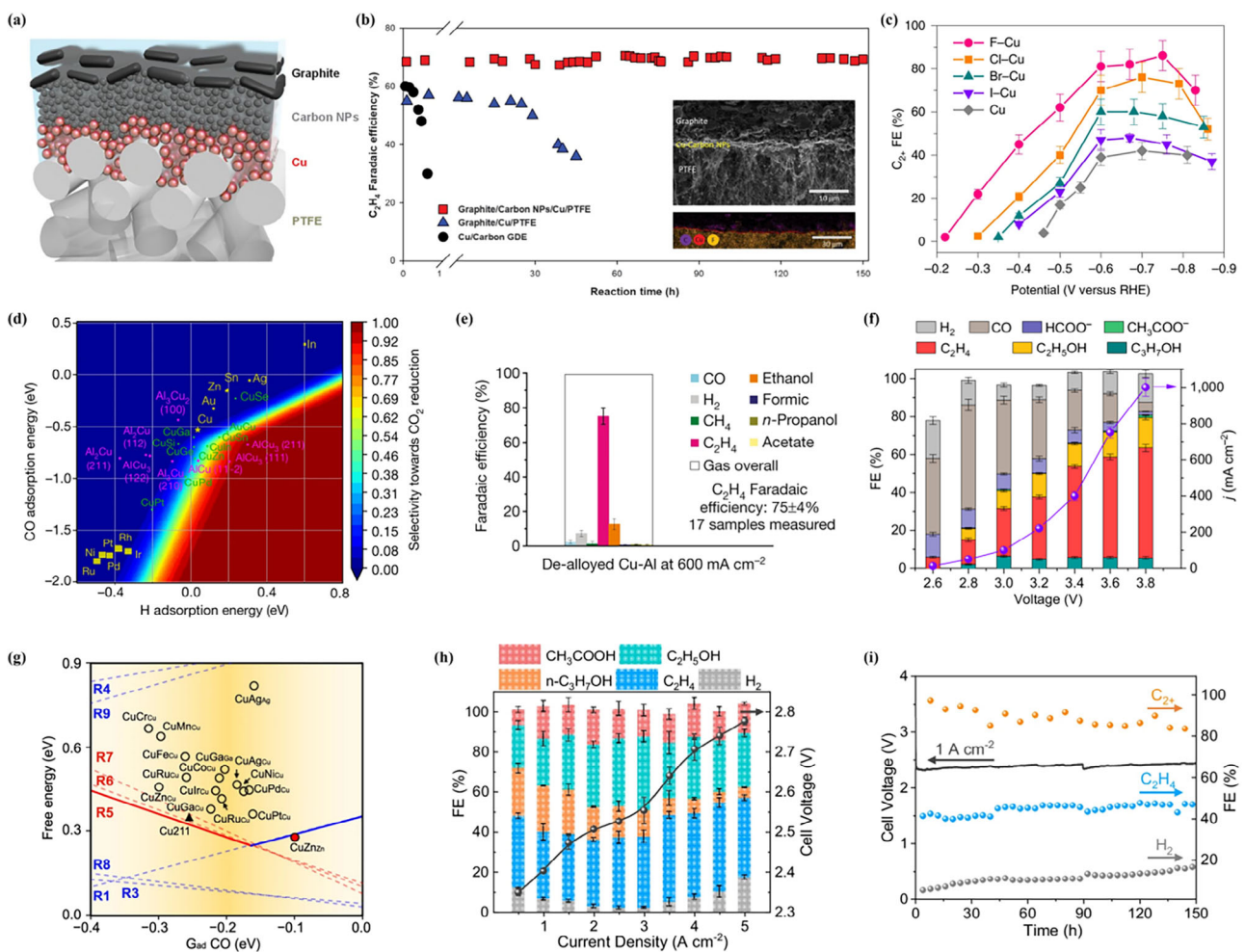


Figure 4. (a) Schematic illustration of the graphite/carbon NPs/Cu/PTFE electrode. (b) Stability test of the polymer-based electrode for CO_2 -to- C_2H_4 conversion in 7 M KOH at -0.55 V vs. RHE. Insets show the cross-section SEM and EDX mapping of the sample after 150 h of continuous operation.^[32] Copyright 2018, AAAS. (c) The FEs of C_2+ products under different applied potentials over X–Cu (where X = F, Cl, Br or I) catalysts in 1 M KOH.^[43] Copyright 2020, Springer Nature. (d) Selectivity volcano plot for CO_2 reduction, showing DFT-calculated CO and H adsorption energies. Yellow: mono-metallics; green: copper alloys; magenta: Cu-Al surfaces. (e) FEs for all products at an applied current density of 600 mA cm^{-2} with 17 de-alloyed Cu-Al samples measured.^[34] Copyright 2020, Springer Nature. (f) FEs of products and the current density over the $Cu^+–Cu^\circ$ catalyst in the presence of co-feeding water with a pressure of 2.7 kPa.^[49] Copyright 2024, Springer Nature. (g) Reaction phase diagram for CO_2 reduction to C_2+ products at -0.6 V vs. RHE. Dashed lines indicate reaction free energies for C–C coupling (red) and protonation steps (blue), while solid lines represent G_{RPD} -limiting steps. Triangles and circles denote limiting energies; black-filled triangle and red-filled circle refer to the reaction energy for Cu_{211} and $CuZn_{2n}$ sites.^[35] Copyright 2023, Springer Nature. (h) Electrochemical CO reduction performance of the Cu nanoparticle (Cu-nc) catalyst, showing FEs and cell voltage as a function of current density. (i) Stability test at a current density of 1.0 A cm^{-2} .^[50] Copyright 2024, Springer Nature.

et al. reported a fluorine-modified Cu (F–Cu) catalyst that achieved an 80% FE for C_2+ products (primarily C_2H_4 and C_2H_5OH) at 1.6 A cm^{-2} (Figure 4c). Fluorine not only enhanced the formation of *H from water but also increased $Cu^{\delta+}$ site density, thus promoting CO adsorption and a hydrogen-assisted C–C coupling pathway.^[43] Similarly, Yan et al. demonstrated that nitrogen doping into Cu_2O improves CO_2 adsorption and intermediate stabilization, resulting in a twofold increase in C_2H_4 yield.^[46] In molecular catalysis, Sargent et al. utilized electro-dimerization of arylpyridiniums on Cu to stabilize CO intermediates, achieving a 72% FE for C_2H_4 with sustained production over 190 h.^[47] Furthermore, Hoang et al. engineered Cu-DAT nanowires with organic modifiers to promote C_1 intermediate adsorption, boosting C_2+ selectivity.^[48] Despite these

advances, Cu surfaces often reconstruct into less active Cu(111) domains, $Cu^{\delta+}$ species are reduced to metallic Cu, or dopants such as halides leach out—all of which increase the competing HER, and requires further advancements to improve the Cu stability.

In addition, insufficient H_2O at the interface has been found to be detrimental to the CO_2R performance. To address the potential issue of H_2O depletion at high current densities in MEA electrolyzers, Wang et al. co-fed CO_2 and H_2O gases to the cathode, achieving excellent C_2+ product performance using a Cu_2O –Cu° catalyst. In their MEA system, an impressive C_2+ FE of 80% was achieved at a current density of 1.0 A cm^{-2} , with ethylene accounting for approximately 60% of the total FE (Figure 4f). Their study revealed that Cu⁺ species facilitate

water activation and C–C coupling by promoting the formation of adsorbed CO and CHO intermediates.^[49]

The electrochemical CO₂-to-CO-to-C₂H₄ tandem route has attracted considerable attention. Wang et al. reported that grain boundary-rich Cu nanoparticles in an alkaline MEA electrolyzer enabled a remarkable C₂₊ partial current density of 4.35 A cm⁻² with a C₂₊ FE of 87 ± 1% and CO conversion of 85 ± 3%, all achieved at a low cell voltage of 2.78 V (Figure 4h). Impressively, the system demonstrated stable operation for 150 h at a high current density of 1.0 A cm⁻² (Figure 4i).^[50]

2.2.2. Acetate

Among C₂₊ products derived from CO₂/CO electroreduction, acetate or acetic acid stands out as a valuable oxygenated chemical with widespread industrial applications in solvents, polymers, and pharmaceuticals. However, achieving high acetate selectivity remains challenging due to competing C–C coupling and protonation pathways that often favor C₂H₄ or C₂H₅OH generation. Given that *CO–COH is a widely proposed intermediate in the formation of C₂₊ products, Kang et al. specifically investigated the reaction pathway leading to acetic acid. Starting from *CO–COH, they proposed a stepwise mechanism involving water-assisted proton–electron transfers: *CO–COH + H₂O + e⁻ → *C–CO + H₂O + OH⁻, *C–CO + H₂O + e⁻ → *CH–CO + OH⁻, *CH–CO + H₂O + e⁻ → *CH₂–CO + OH⁻, *CH₂–CO + H₂O → CH₃–COOH (Figure 5a).^[51] This mechanistic proposal offers valuable insight into selective pathways for acetate formation among C₂₊ products. However, the actual reaction route can vary significantly depending on the catalyst structure and reaction environment, as other studies have reported different intermediates or rate-determining steps.

Catalysts based on Cu have demonstrated great potential for the electroreduction of CO₂ to acetate. The primary strategies focus on constructing efficient reduction sites, tailoring the reaction microenvironment, and modulating intermediate reaction pathways to steer product selectivity. For instance, Han et al. developed a sheet-like N-based Cu(I)/C-doped boron nitride (BN-C) composite, which achieved a remarkable acetate FE of 80.3% at a current density of 13.9 mA cm⁻².^[52] In another approach, Chen et al. employed a 2D phthalocyanine-based covalent organic framework (COF) as the electrocatalyst (PcCu-TFPN). Operating at –0.8 V vs. RHE in 0.1 M KHCO₃, the system reached an acetate FE of 90% with a current density of 12.5 mA cm⁻², exhibiting excellent selectivity and long-term stability.^[53] Recently, Zhu et al. introduced a spherical self-pressurizing nanoscale capsule catalyst, which generates a high-pressure CO intermediate environment around Cu through a permselective shell. This design promotes a CO–CO₂ coupling pathway via the COCO₂* intermediate, achieving 38.5 ± 2.2% FE and a record acetate partial current density of 328 ± 19 mA cm⁻² under high-rate conditions.^[54]

Moreover, in addition to multi-carbon products, asymmetric adsorption site design also offers significant advantages in the formation of multi-carbon oxygenated compounds. By creating asymmetric binding environments that favor specific

reaction pathways, catalysts with tailored adsorption sites can effectively guide the conversion of CO₂/CO to desired products, thereby optimizing the overall electrocatalytic process. Building on the asymmetric adsorption strategy, adjusting the surface coverage of CO reactants can steer product selectivity. Sargent et al. achieved a 70% selectivity for acetate via a two-step electrochemical synthesis strategy starting from CO. By tuning the ratio of Ag in Ag–Cu₂O catalysts, they effectively suppressed the formation of ethylene and ethanol, highlighting the crucial role of heterointerfaces in steering product selectivity (Figure 5b,c).^[55] The surface coverage of *CO has been identified as a key factor in steering the selectivity toward acetate production. Pang et al. adjusted CO pressure to modulate *CO coverage, increasing contact between ketene intermediate and alkaline electrolyte, achieving over 90% selectivity toward acetic acid (Figure 5d).^[56] Similarly, Zheng et al. developed a Cu–Pd catalyst where increased CO coverage and stabilized ethenone intermediates achieved over 70% acetic acid selectivity (Figure 5e).^[57] Gao et al. developed a crystalline-amorphous copper catalyst modified with cerium single atoms (Ce-SAs/Cu). Under pulsed electrolysis conditions, the catalyst achieved a maximum acetate FE of 71.3 ± 2.1% with an averaged partial current density of 110.6 ± 1.9 mA cm⁻² for acetate production (Figure 5f).^[58] Zeng et al. employed a thick anion exchange membrane in a porous solid electrolyte reactor to slow down alcohols crossover. As a result, an acetic acid solution with a relative purity of ~97 wt.% was produced over 140 h at a current density of –250 mA cm⁻² (Figure 5g).^[59] To achieve stable acetate production under industrially relevant conditions, Huang et al. designed a Zeolite Socony Mobil-confined Cu single-atom cluster (CuZSM SACL). This catalyst enabled over 70% selectivity toward acetate at ampere-level current densities. The strong Cu–O–Si coordination within the zeolite framework stabilized the dispersed single Cu atoms, ensuring operational stability exceeding 1000 h (Figure 5h).^[60] In addition, Jiao et al. demonstrated a tandem CO₂ electrolyzer for the production of multcarbon products, acetate, and ethylene, scaled to the kilowatt (kW) level. Drawing on insights obtained at the watt scale, they have designed and operated a 0.71 kW, 1000 cm² CO electrolyzer and a 0.40 kW, 500 cm² CO₂ electrolyzer. The kW-scale CO electrolyzer stably produced a current of 300 A over 125 h, generating 98 L of 1.2 M acetate with 96% purity. These results marked a significant advancement in the industrial feasibility of tandem CO₂ electrolysis systems. A TEA based on experiments was provided. The largest potential for cost reduction lies in energy utilization, which can be achieved by reducing the cell voltage from 2.26 V to 2.1 V and increasing the FE from 37% to 65% at 300 mA cm⁻² (Figure 5i).^[61] These improvements would reduce the cost of electrochemical acetate production. Moreover, reduced electricity usage, optimized auxiliary processes, and tax credits provide a viable route for acetate production via tandem CO₂ electrolysis with economic feasibility.

2.2.3. Ethanol and n-Propanol

C₂H₅OH is a valuable liquid fuel and chemical feedstock with extensive industrial applications. Current C₂H₅OH production

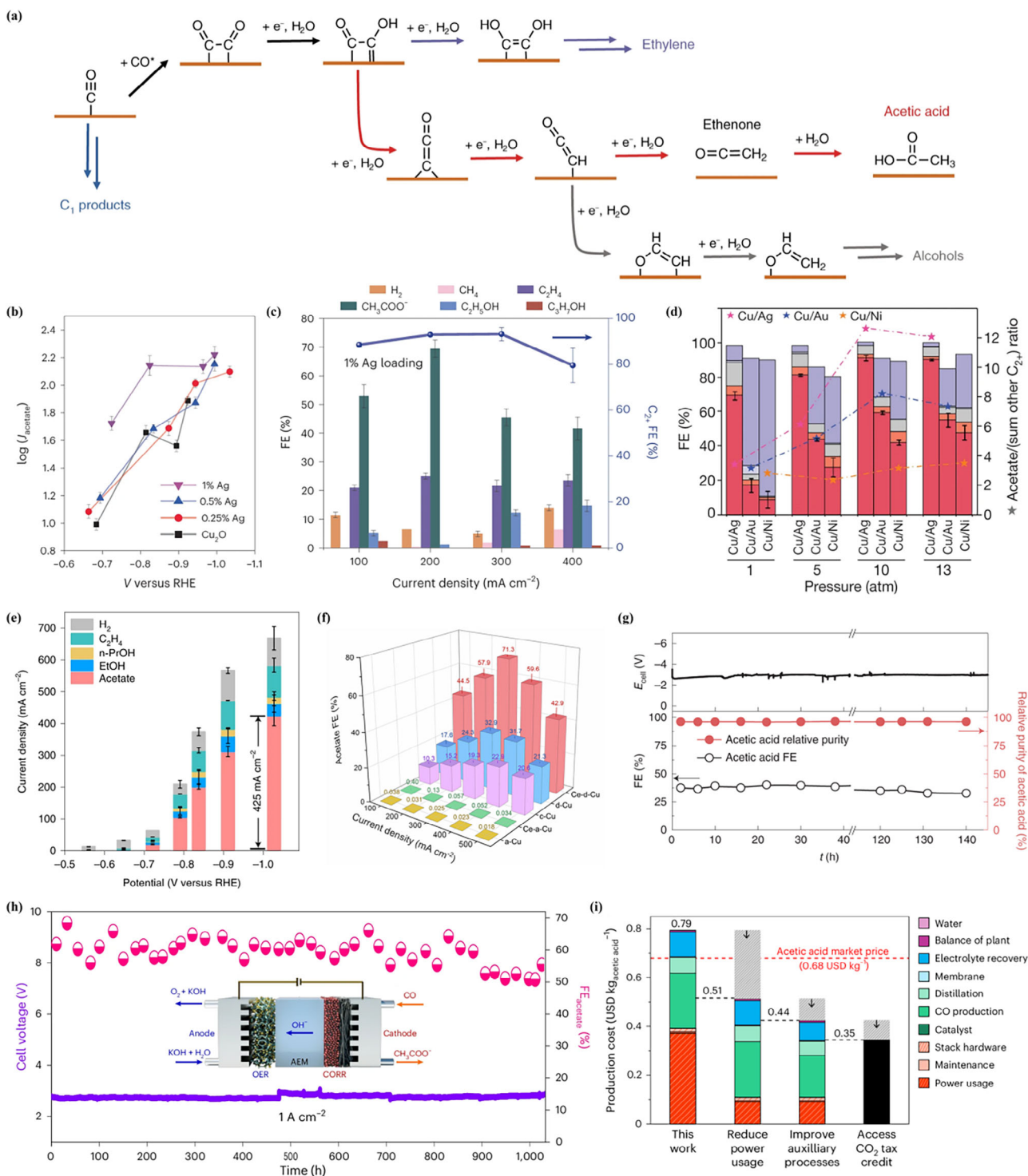


Figure 5. (a) Proposed mechanism for the electroreduction of CO to C_{2+} products based on DFT.^[51] Copyright 2019, Springer Nature. (b) Acetate partial current densities of C_2 products for the Cu_2O and 0.25, 0.5 and 1% Ag– Cu_2O catalysts. (c) FE distribution of the CORR products for the $Ag_{19\%}-Cu_2O$ catalyst at different current densities.^[55] Copyright 2023, Springer Nature. (d) Effect of host metal on CO electroreduction over Cu/M-DA materials under pressure.^[56] Copyright 2023, Springer Nature. (e) Current densities of each CORR product and H_2 on CuPd at different applied potentials in 1 M KOH.^[57] Copyright 2022, Springer Nature. (f) Acetate FE on various CuCe-based catalysts at cathodic current densities ranging from 100 to 500 $mA\ cm^{-2}$.^[58] Copyright 2025, Springer Nature. (g) Long-term operation of CO reduction to acetic acid solution under $\sim 250\ mA\ cm^{-2}$. The FE and relative purity of acetic acid were maintained over the 140 h of continuous operation (t , time).^[59] Copyright 2022, Springer Nature. (h) FEs of Zeolite Socony Mobil-confined Cu single-atom cluster (CuZSM SACL)-based MEA with CORR products at different current densities in 5 M KOH.^[60] Copyright 2025, Springer Nature. (i) Roadmap outlining strategies to reduce the cost of electrochemical acetic acid production below the current market price (gray regions with arrows indicate the direction of cost reduction).^[61] Copyright 2024, Springer Nature.

heavily relies on fossil-derived C_2H_4 hydration or biomass fermentation, facing challenges in energy efficiency and carbon footprint.^[62] Electrocatalytic CO_2R to C_2H_5OH offers a sustainable alternative by under mild conditions.^[63,64] Recent advances in catalyst design and microenvironment engineering have demonstrated promising routes to steer CO_2 -to- C_2H_5OH conversion.

The selective formation of C_2H_5OH requires efficient stabilization of oxygenated intermediates on the catalyst surface. A key branching intermediate is $CH_2=CHO^*$, adsorbed via a Cu—O—C linkage, where subsequent cleavage of either the Cu—O or O—C bond directs the reaction toward C_2H_5OH or C_2H_4 , respectively, rendering this bifurcation point critical for product selectivity.^[63] Molecular modification has emerged as effective approaches to modulate the adsorption and transformation of key intermediates in electrocatalytic reactions. Zheng et al. engineered copper catalysts through surface nitrosamine functionalization, enhancing electronic delocalization to weaken and cleave the Cu—O bond within the adsorbed $CH_2=CHO^*$ intermediate (Figure 6a). Consequently, a CO_2 -to-ethanol FE of 45% was achieved. In a MEA system, the catalyst demonstrated operational stability for over 300 h at an industrial current density of 400 mA cm^{-2} (Figure 6b).^[63] Han et al. synthesized a multivalent copper-based catalyst, Cu-2,3,7,8-tetraaminophenazine-1,4,6,9-tetraone (Cu-TAPT), which leverages the synergistic effect of Cu^{2+} and Cu^+ active sites to promote asymmetric C—C coupling (Figure 6c). This facilitates the formation of hydroxyl-containing C_2 intermediates (e.g., HCCHOH) and favors ethanol production. At an industrially relevant current density of 429 mA cm^{-2} , Cu-TAPT achieved an ethanol FE of $54.3 \pm 3\%$ (Figure 6d).^[65] Asymmetric site design also benefits the formation of C_{2+} oxygenates like alcohols, aldehydes, and acids. Wang and Qiao et al. developed a Ag-modified Cu oxide catalyst ($Cu_2O/Ag_{2.3\%}$) that enabled dual atop and bridge $*CO$ adsorption configurations, achieving 40.8% FE and 22.3% EE for C_2H_5OH at 326.4 cm^{-2} at -0.87 V .^[66] Inspired by the Wood-Ljungdahl pathway, Chen et al. employed a Cu—Ag electrocatalyst to promote asymmetric C—C coupling between $*CH_3$ and $*CO$ intermediates, favoring oxygenate formation (e.g., acetaldehyde, ethanol, acetic acid, acetone). By tuning the Cu/Ag nanoparticle ratio, they optimized the formation kinetics of $*CH_x$ ($x = 1-3$) and $*CO$, enhancing oxygenate selectivity.^[67] Notably, Burdyny et al. employed a non-Cu-based catalyst to achieve CO_2 conversion to ethanol, demonstrating the feasibility of alternative catalytic materials beyond traditional copper systems. Using a heterogenized nickel-loaded iron tetraphenylporphyrin electrocatalyst, a FE of $68\% \pm 3.2\%$ for ethanol production was achieved, along with a partial ethanol current density of 21 mA cm^{-2} .^[68] Collectively, these studies investigated molecular catalysts and asymmetric binding mechanisms in promoting C_2H_5OH formation. Huang et al. reported a Cu-free, Sn-based electrocatalyst that achieved a maximum ethanol selectivity of $\sim 82.5\%$ at 0.9 V_{RHE} using a catalyst that consists of SnS_2 nanosheets and single-Sn atoms anchored on a 3D carbon support via a local SnO_3 cluster (SnS_2/Sn_1-O3G) (Figure 6e).^[69]

n-Propanol is a valuable oxygenate product and gains research interest.^[70] The formation of C_3 products relies on sequential C_1-C_1 and C_2-C_1 coupling steps, with a critical bifurcation point arising from the interaction between C_1 and C_2 intermediates—determining whether the reaction proceeds to C_2 or C_3 products. A prerequisite for high C_3 yields is the stabilization of C_2 intermediates on catalyst surfaces, enabling their subsequent coupling with adsorbed CO. In the case of n-propanol production, this requires precise tuning the adsorption behavior of oxygenated intermediates. Introducing Lewis acid sites on Cu surfaces provides a means to modulate such adsorption and promote C—O bond cleavage. Yang et al. designed a cooperative electrocatalyst by anchoring atomically dispersed Lewis acidic Zr(IV) species onto Cu (denoted as a-Zr/Cu), which facilitated the electrochemical reduction of CO_2 to n-propanol. The resulting a-Zr/Cu catalyst exhibited an excellent FE of $14.4 \pm 0.3\%$ and a partial current density of $-70 \pm 1.0\text{ mA cm}^{-2}$ at -0.80 V vs. RHE.^[71]

The development of coordinatively unsaturated Cu sites is crucial for enhancing C_3 product formation by facilitating $*CO$ dimerization and stabilizing $*C_2$ intermediates to boost C_1-C_2 coupling. Li and co-workers designed an ultra-low coordinated Cu catalyst by in situ reducing CuO NPs confined within an ordered porous matrix (Figure 6f). This strategy led to a remarkable FE for n-PrOH production, reaching 27.4% at -0.8 V vs. RHE in an H-cell and 11.8% at 300 mA cm^{-2} in a flow cell.^[72] Similarly, through structural design, Gao et al. synthesized porous Cu_2O spheres using an acid etching method. Finite element simulations indicated that this nanostructure confines intermediates and protects Cu^+ during CO_2R (Figure 6g), thereby achieving efficient CO_2R for the production of C_{2+} fuels (75.2% FE with C_{2+} current density of $267 \pm 13\text{ mA cm}^{-2}$).^[73] Bhoumik et al. designed a Cu/Cys/Au bimetallic catalyst, leveraging the synergistic effects between the weak CO adsorption capability of Au and the strong C—C coupling ability of Cu, achieving a FE of 29.1% for n-propanol at -1.2 V versus RHE during CO_2 electroreduction.^[74]

With the rising accessibility of CO as a feedstock—enabled by advancements in CO_2 -to-CO conversion—the cascade pathway of CO_2 reduction to CO followed by CO electroreduction (COR) to n-propanol has attracted attention. Sargent and co-workers proposed that while adsorbed CO is a key intermediate to C_2 products, formyl (CHO) and formaldehyde (CH_2O)-related intermediates serve as critical C_1 precursors in the n-propanol formation pathway (Figure 6h). To promote the generation and stabilization of these oxygen-containing intermediates, they introduced a second metal with higher oxophilicity than Cu into the catalyst design. Integrating this strategy with advanced electrode engineering, they developed a compositionally controlled, heterostructured Sn—Cu dilute alloy catalyst (termed CCIH), which achieved a FE of $47 \pm 3\%$ for n-propanol, a single-pass CO conversion of 88%, and an electrolyzer EE of 24% at 150 mA cm^{-2} , with stable operation for 120 h in a MEA electrolyzer. Additionally, the formation of a catalyst/carbon/ionomer heterojunction structure facilitated reverse electro-osmotic

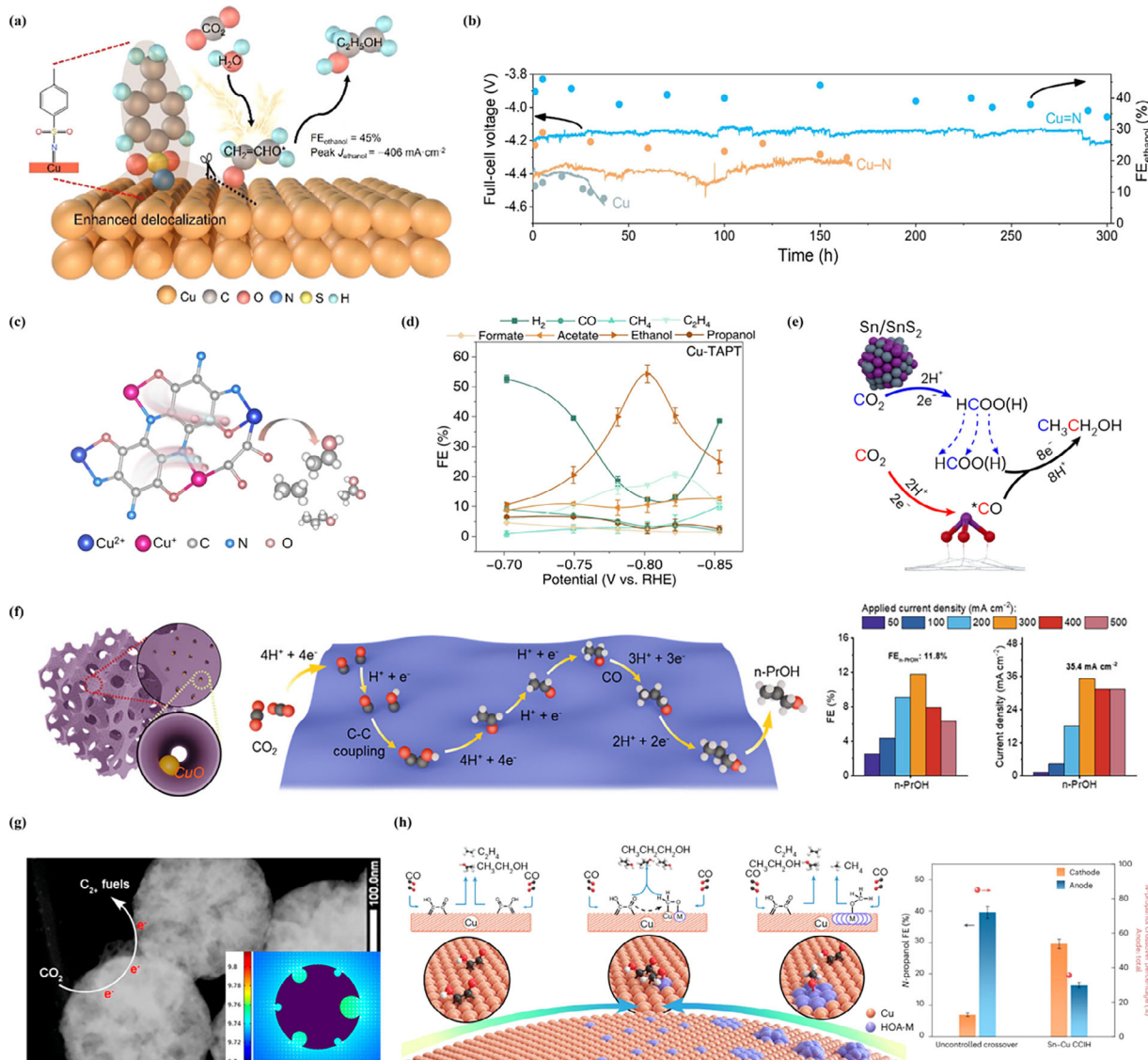


Figure 6. (a) Nitrene functionalization of the Cu catalyst enables an electron delocalization tuning strategy, which allows weakening and cleaving of the $\text{Cu}-\text{O}$ bond of the adsorbed $\text{CH}_2=\text{CHO}$, and promotes C=C hydrogenation along the ethanol pathway. (b) Stability test of the Cu, Cu—N, and Cu=N catalysts in a 5 cm^2 MEA electrolyzer under a constant current density of -400 mA cm^{-2} .^[63] Copyright 2024, American Chemical Society. (c) Schematic illustration of C—C coupling formation process on Cu-TAPT based on the synergistic effect of Cu^{2+} and Cu^+ . (d) FEs of all products under different applied potentials over Cu-TAPT in 1M KOH electrolyte.^[65] Copyright 2024, Springer Nature. (e) A schematic illustration showing the cascade reaction during CO_2 reduction to ethanol over SnS_2 nanosheets and single-Sn atoms anchored on a 3D carbon support via a local SnO_3 cluster ($\text{Sn}/\text{SnS}_2/\text{SnO}_3/\text{C}$) (grey: S; red: O; yellow: H and purple: Sn). The C in red and blue colors indicates sources of carbon atoms in ethanol from two sub-reactions.^[69] Copyright 2023, Springer Nature. (f) (Left) Structural schematic diagram of $\text{CuO}/3\text{DOM SiO}_2$. (Middle) Proposed reaction pathways for the C_1-C_2 coupling and the formation of $n\text{-PrOH}$ products. (Right) FE and partial current density of $n\text{-PrOH}$ at different current densities on $\text{CuO}/3\text{DOM SiO}_2$ in the flow cell.^[72] Copyright 2025, American Chemical Society. (g) Morphology and structure characterizations of multihollow Cu_2O catalyst.^[73] Copyright 2024, American Chemical Society. (h) (Left) Tuning HOA-M surface coverage on Cu—based on the atomic arrangement of active sites—to regulate intermediate adsorption and boost C_1-C_2 coupling for improved n -propanol production. (Right) N-propanol FE at cathode and anode sides comparing uncontrolled crossover and Sn—Cu CCIH architecture at 40 °C. Data were collected at 150 mA cm^{-2} in 3 M KOH.^[75] Copyright 2025, Springer Nature.

drag, effectively concentrating the produced n -propanol to 30 wt%.^[75]

3. Interfacial Effects Induced by Electrolytes in CO_2 Electrocatalysis

MEA electrolyzers do not contain catholyte, therefore the surface environment at the cathode is affected by the anolyte and ion

exchange membranes, which modulates local pH, cations, and anions to determine the overall CO_2 R performance of the system.

In MEAs, the local pH at the interface influence the catalytic selectivity, stability, and CO_2 utilization efficiency.^[31] Zhang et al. used *in situ* Raman spectroscopy to monitor the pH near the surface of a Ag catalyst and studied the effects of pH near the catalyst surface as a function of current density during the CO_2 R reaction. They found that elevated current densities led to an increase in surface pH and a reduction in HER (Figure 7a,b).^[76]

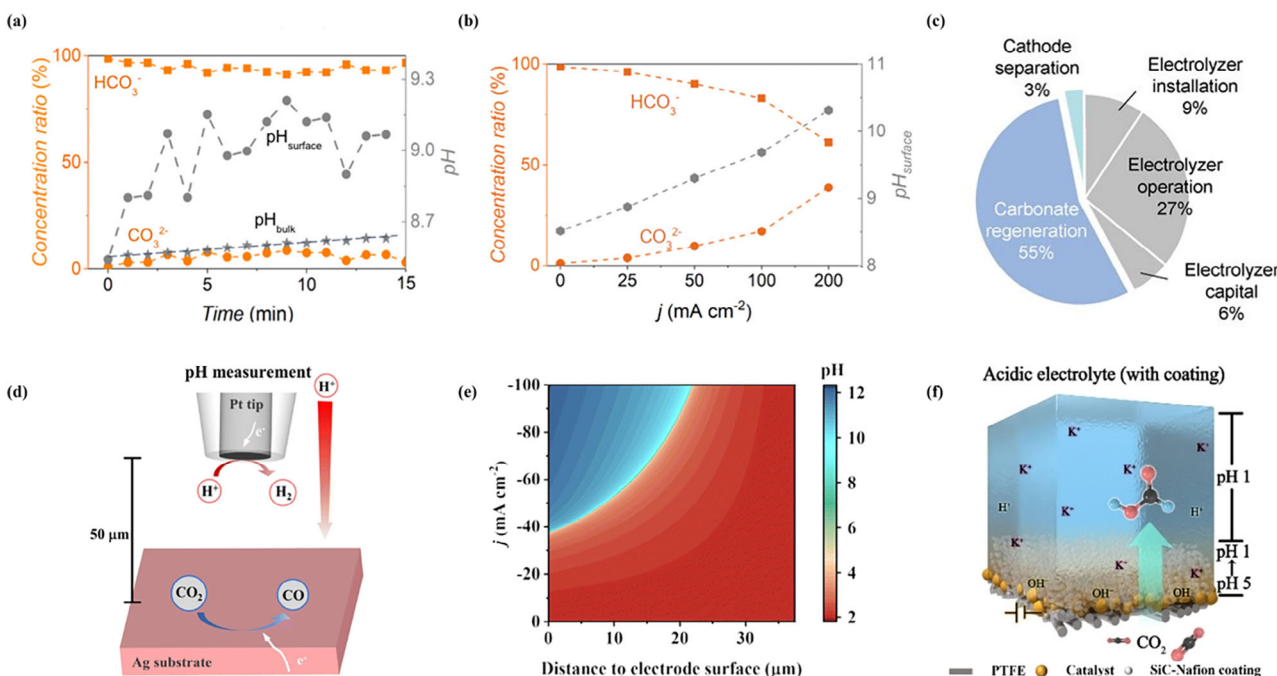


Figure 7. (a) Concentration ratios of HCO_3^- and CO_3^{2-} (orange lines), surface pH calculated using the equilibrium of HCO_3^- and CO_3^{2-} (gray dots), and bulk pH measured by a pH meter (gray stars). (b) Ratios of $[\text{HCO}_3^-]/[\text{C}_{\text{total}}]$ and $[\text{CO}_3^{2-}]/[\text{C}_{\text{total}}]$ and the corresponding calculated pH near the catalyst surface.^[76] Copyright 2020, American Chemical Society. (c) Cost breakdown of an alkaline CO_2R flow cell based on technoeconomic analysis.^[77] Copyright 2021, AAAS. (d) Schematic of pH measurement by scanning electrochemical microscopy (SECM). (e) Simulated pH profile at different current densities at 63 sccm electrolyte flow rate.^[80] Copyright 2024, Royal Society of Chemistry. (f) Application of the SiC-NafionTM coated layer and the resulting regulated pH and ion concentrations near the catalyst surface. Copyright 2023, Wiley-VCH.^[82]

Dinh and Sargent et al. found that increasing the local pH near catalyst surfaces largely enhances the kinetics of CO_2R , particularly for multi-carbon products.^[77] However, Xu et al. pointed out that the promoting effect of alkaline electrolytes on C_{2+} product formation rates may originate from the increased cation concentration rather than the OH^- concentration due to the inappropriate use of the RHE scale for comparison (Figure 8d), which provides a perspective on the role of cations in enhancing CO_2/CO electrocatalytic activity.^[78] Another issue with the use of neutral or alkaline electrolytes is that CO_2 reacts with OH^- to form carbonate or bicarbonate anions leading to substantial CO_2 loss during the CO_2R reaction (over 85% of the input CO_2), which limits the maximum carbon efficiency of CO_2 conversion (Figure 7c).^[77] In addition, CO_2 crossover leads to a decrease of the outlet flow rate from the cathodic compartment.^[79] Conducting CO_2R under acidic conditions can effectively solve this problem. Nonetheless, in acidic electrolytes, the high concentration of H^+ leads to strong HER. Thus, effectively suppressing HER in an acidic electrolyte is crucial for achieving efficient and stable CO_2R with high carbon and energy efficiency. Wang et al. employed scanning electrochemical microscopy (SECM) to investigate the impact of a local environment, distinct from the bulk solution, on CO_2R under mildly acidic conditions with local pH near the surface being natural (Figure 7d,e).^[80] They argue that it remains challenging to suppress HER while keeping the local pH below the pK_a of carbonic acid. To address this, they suggest that achieving a carbonate-free interface in acidic media, devoid of metal cations, is essential to remove the counterion for salt.

Previous studies have also modulated the microstructure of the three-phase reaction interface to regulate the local pH for enhanced CO_2R performance. Yang et al. showed that Cu mesoporous electrodes have morphological effects in the selective production of C_2 products, and that CO_2 can be selectively converted to C_2H_4 or C_2H_6 by controlling the Cu mesopore size. Supported by computational simulations, their study demonstrated that nanomorphology changes the local pH.^[81] Furthermore, this effect is more pronounced when implementing a stratified cathode design that incorporates an electrically nonconductive SiC coating on active Sn-Bi catalysts. Li and Zhong et al. reported a pH graduation model to visualize the local microenvironment at the interface (Figure 7f). In the reports, by coating catalysts with an electrically nonconductive nanoporous SiC-Nafion layer, a near-neutral pH was stabilized on catalyst surfaces, thereby CO_2 -to-HCOOH was achieved with a FE of HCOOH up to 90%, and the SPCE >70% at 100 mA cm⁻² at pH 1.^[82] Additionally, Liu et al. constructed Ni@NCN yolk–shell nanoreactors, which showed CO_2R to CO selectivities of 93.2% and 84.3% under acidic (pH = 2.5) and neutral (pH = 7.2) conditions, respectively. The consumption of H^+ in the liquid film at the catalyst surfaces increases the local alkalinity. The nanoporous structure hinders the outward diffusion of the locally generated OH^- , suppressing HER and consequently increasing CO_2R in bulk acidic conditions.^[83] Moradzaman et al. demonstrated that tuning anions in a 0.1 mol/L solution significantly influenced CO_2R selectivity on Cu, increasing C_2H_4 FE from 5.2% in KH_2PO_4 solution to 43.2% in KOH solution. This was attributed to anion buffering capacity and local pH,

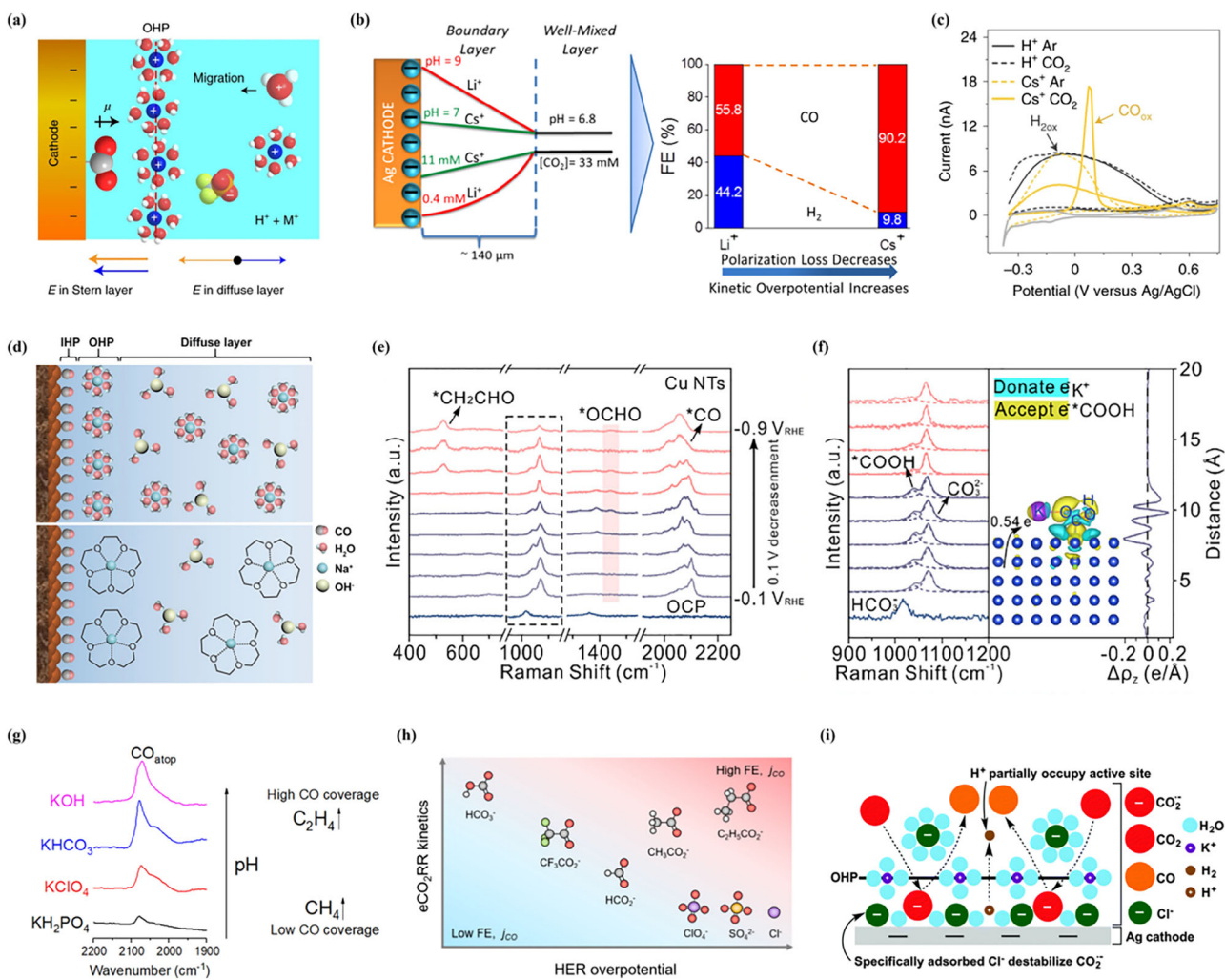


Figure 8. (a) Schemata of double layer near cathode in HOTf + MOTf media.^[86] Copyright 2022, Springer Nature. (b) Effect of cation hydrolysis on CO_2 electroreduction over Ag: pH and CO_2 distribution in the boundary layer with larger cations enhancing CO selectivity and suppressing H_2 evolution via reduced polarization.^[89] Copyright 2016, American Chemical Society. (c) CO detection with SECM: CV of the Pt-UME after CO_2 reduction on Cu electrodes, with reference CV shown in light grey.^[90] Copyright 2021, Springer Nature. (d) A schematic representation of the decrease of cations in OHP owing to the chelation by 15-crown-5. IHP is the inner Helmholtz plane and OHP is the outer Helmholtz plane.^[78] Copyright 2020, American Chemical Society. (e) In situ Raman spectra from the Cu NTs at varying potentials. (f) Enlarged Raman spectra depicting the $^{*}\text{COOH}$ modes for the Cu NTs and corresponding charge density distributions of the adsorbed $^{*}\text{COOH}$ on Cu in the presence and absence of K^+ , respectively.^[93] Copyright 2025, Wiley-VCH. (g) The schematic illustrates how different anions regulate surface pH and the coverage of CO intermediates.^[84] Copyright 2021, American Chemical Society. (h) Effect of various inorganic and carboxylate anions on the selectivity and activity of electrocatalytic CO_2 reduction on gold catalysts, illustrated by overpotentials for HER and CO_2R .^[95] Copyright 2024, American Chemical Society. (i) Schematic illustrations of processes in the double layer that play a role in the kinetics of CO_2 to CO conversion on an Ag cathode when using KCl as the electrolyte.^[96] Copyright 2016, Royal Society of Chemistry.

with in situ ATR-SEIRAS confirming that higher pH enhances CO coverage (Figure 8g).^[84] Despite these advances, further efforts are needed to identify the optimal local pH in combination with an enhanced reaction environment that promotes CO_2R over competing reactions.

The promoting role of cations in CO_2R has been extensively documented. For instance, on Cu electrodes, the selectivity toward C_2+ products increases with the size of alkali metal cations ($\text{Li}^+ < \text{Na}^+ < \text{K}^+ < \text{Rb}^+ < \text{Cs}^+$).^[85] Despite these consistent experimental observations, the mechanistic origins of such cation-dependent trends remain controversial and thus are actively investigated. It has been reported that the introduction of basic cations (such as K^+) during CO_2R enhances the electric

field in the Stern layer (Figure 8a),^[86] which is related to both the cation size and the structure of their hydration shells.^[87] Cations with smaller hydration shells, such as Cs^+ , approach the catalyst surface more closely, allowing for greater charge accumulation in the Stern region. This leads to the formation of a stronger interfacial electric field.^[88] Compared to monovalent alkali metal cations, multivalent cations (e.g., Be^{2+} , Mg^{2+} , Ca^{2+} , Ba^{2+} , Al^{3+} , Nd^{3+} , and Ce^{3+}) affect CO_2R , but the overall effect is less significant than that of alkali metal cations.^[88] Singh et al. proposed an alternative theoretical framework, suggesting that cations influence CO_2R by buffering the interfacial pH.^[89] In addition, using scanning electrochemical microscopy (SECM), Koper et al. confirmed the role of metal cations in stabilizing key CO_2R

intermediates via electrostatic interactions (Figure 8c). They proposed that in the absence of solvated metal cations, CO₂R does not proceed.^[90] However, recent studies have demonstrated that efficient and stable CO₂R to C₂H₄ can be achieved in MEA electrolyzers using pure water as the electrolyte, challenging the understanding of cation-dependent CO₂R mechanisms.^[91,92] Recently, Hao et al. developed clean Cu nanoparticles with tailored curvature to modulate the local concentration of K⁺ ions and investigate their effects on CO₂R (Figure 8e,f). For Cu nanotips (Cu NTs), the optimal potential for C₂ product formation appeared earlier than typically observed, likely due to the ultra-high local K⁺ concentration induced by the tip effect.^[93] This work leveraged the promotional role of cations from a catalyst design perspective, offering a broad tunability of local cation concentration without the constraints of solubility limits or anion interference.

In addition, anions also play a crucial role in CO₂R selectivity. For example, the use of KCl, K₂SO₄, KClO₄, and dilute KHCO₃ solutions as electrolytes favor the formation of C₂H₄ and C₂H₅OH.^[94] Lukatskaya et al. employed *in situ* differential electrochemical mass spectrometry (DEMS) for real-time product analysis, coupled with molecular dynamics (MD) simulations, to investigate how various inorganic and carboxylate anions influence the selectivity and activity of electrocatalytic CO₂R on gold catalysts (Figure 8h).^[95] They found that anions with weaker physisorption free energies facilitate favorable CO₂R kinetics, despite the negatively charged electrode surface. Based on this insight, propionate was identified as a promising anion, exhibiting CO production rates comparable to those achieved with bicarbonate. Halide ions are among the most extensively studied anions for specific adsorption (Figure 8i).^[96] This interaction increases the negative charge on the electrode surface. Additionally, computational calculations support the adsorption of Cl⁻, Br⁻, and I⁻ on Cu surfaces at the potential commonly used for CO₂R reactions. The anion effect affects the onset potential of CO₂R to CO, and the following law was obtained: OH⁻ (-0.13 V vs. RHE) < HCO₃⁻ (-0.46 V vs. RHE) < Cl⁻ (-0.60 V vs. RHE), because the anion species affects the catalyst surface CO₂ distribution, local pH concentration, Ohmic resistance, etc., and thus have an impact on the performance of electrocatalytic CO₂R.^[97]

4. Gas Diffusion Electrodes

GDE plays a critical role as a fundamental component in the MEA device (Figure 1b), as it facilitates the transport of CO₂ to the catalyst surface. The GDE is typically constructed using a porous GDL, which can be made from carbon materials or PTFE, with the electrocatalysts coated on the hydrophobic surface of the diffusion layer (Figure 9a).^[98] To ensure sustained catalytic performance, maintaining a stable three-phase interface on the GDE is essential. This requires the GDL to have sufficient hydrophobicity to ensure consistent gas transport. However, when alkaline electrolytes containing cations such as K⁺ are used, carbonate precipitation on the GDL side becomes a signif-

icant issue, potentially blocking gas channels and compromising long-term operation.

Traditional carbon-based GDLs are designed as either a single microporous layer or a bilayer structure. The latter consists of a microporous layer coated with a thinner microporous layer. The microporous layer is constructed from interconnected carbon fibers, creating pores larger than 10 μm. In contrast, the microporous layer is composed of carbon powders and hydrophobic agents, forming smaller hydrophobic pores (<0.1 μm). The carbon powder in the microporous layer can infiltrate the microporous layer, creating an interlocking interface that enhances structural stability and provides a conductive medium. As shown in Figure 9a, this bilayer design is commonly preferred in MEAs. This is because the smaller pores in the microporous layer require higher breakthrough pressures to become flooded, as predicted by the Young-Laplace equation, which improves water management during CO₂R.^[99] Another type of porous PTFE-based GDL material exhibits better hydrophobicity and stability during CO₂R (Figure 9a). However, due to its inherent lack of conductivity, it typically requires the catalyst layer to possess good electrical conductivity or the addition of a carbon layer between the GDL and CL to enhance conductivity.

Studies are dedicated to enhancing the hydrophobicity of GDEs to optimize CO₂ transport efficiency and maintain the stability of the hydrophobic structure. Without sufficient CO₂ transport, the HER dominates over CO₂R. For a more detailed understanding of the dynamics within the GDE, Ozden and Sargent et al. observed a positive correlation between the current density of CO₂R and the supplied CO₂ partial pressure (Figure 9b), which suggests that the concentration of local CO₂ available at the catalyst surfaces plays a crucial role in the CO₂R reaction.^[100] Research on PTFE-modified hydrophobic Cu catalysts has shown that, according to the Young-Laplace equation, the smaller pore size of the PTFE substrate maintains a higher capillary pressure difference at the water-air interface.^[99] Beyond adjusting pore diameters, researchers have focused on enhancing the hydrophobicity of catalyst surfaces to further promote the efficiency of CO₂ reduction.^[101,102] Furthermore, studies have explored the impact of functional groups on Cu electrodes, revealing that polymers with protic species and hydrophilic groups enhance H₂ and HCOOH selectivity, while cationic hydrophobic species improve CO selectivity, providing valuable insights for surface modifications in CO₂R.^[103,104]

The role of H₂O present on the catalyst surface of GDE is crucial, as it acts as a proton source for CO₂R. H₂O originates from either the humidified CO₂ side or penetrate from the anolyte. In this regard, Yun Jeong Hwang et al. studied the role of water supply in MEAs for C₂H₄ production using deuterium-labeled water (Figure 9c). Their findings indicated that C—H bond formation in CO₂R primarily depends on water transported through the membrane, whereas humidified water in the CO₂ feed mainly influences the catalytic environment and water activity to ensure sufficient water on the surfaces.^[105] Moreover, based on computational fluid dynamics (CFD) simulations, in regions where CO₂R is dominant, the kinetics of C₂H₄ production strongly depended on the water activity of the catalyst. Consistent with these findings, Weber's simulations

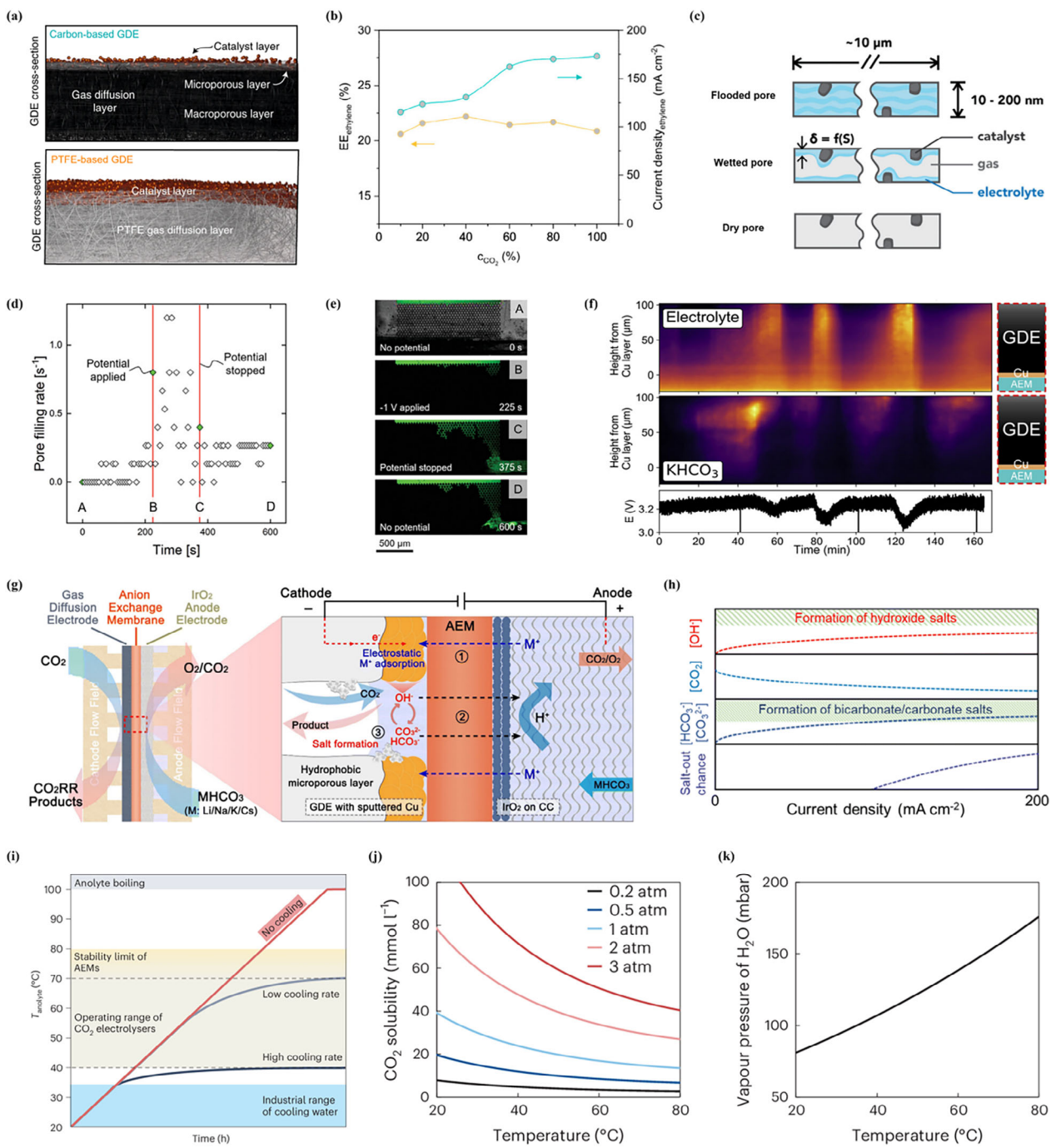


Figure 9. (a) Schematic of two types of GDE structures: carbon-based and polytetrafluoroethylene (PTFE)-based.^[98] Copyright 2022, Springer Nature. (b) Full-cell EEs and ethylene partial current densities as a function of CO_2 concentration in a diluted CO_2 stream from the 3D CTPI catalyst in an MEA electrolyzer.^[100] Copyright 2020, American Chemical Society. (c) Schematic of pore conditions in the catalyst layer. Flooded pore: pore volume filled with electrolyte. Wetted pore: a thin layer of electrolyte covers the pore walls. Dry pore: catalyst inactive due to lack of an ionic pathway.^[110] Copyright 2018, Royal Society of Chemistry. The electrowetting phenomenon including (d) the electrowetting pore filling rate of GDE over time, (e) the corresponding confocal laser scanning microscopy (CLSM) images.^[109] Copyright 2022, Wiley-VCH. (f) The observation of electrolyte penetrating and salt precipitation in a GDE over electrolysis at 100 mA cm^{-2} . The wide-angle X-ray scattering (WAXS) was used to quantify the electrolyte and (bi)carbonates content during electrolysis, where the color from purple to yellow indicates the increase of X-ray intensity of electrolyte and KHCO_3 .^[113] Copyright 2023, Elsevier. (g) Schematic of a zero-gap AEM-based CO_2 electrolyzer illustrating cation (M^+) movement, anion ($\text{OH}^-/\text{HCO}_3^-/\text{CO}_3^{2-}$) diffusion, and salt formation at the cathode GDE. (h) Species concentration changes and salt precipitation likelihood at the cathode GDE with current density (dashed lines are inferred from experiments).^[111] Copyright 2023, Royal Society of Chemistry. (i) Development of the anolyte temperature T_{anolyte} over operation time. The maximum anolyte temperature is imposed by the AEM stability. The electrolyte temperature at the electrolyser inlet (T_{in}) is equal to T_{anolyte} and is lower than the outlet temperature of the electrolyser (T_{out}). The minimum temperature is given by the temperature level T_{cool} and the applicable cooling rate of the heat exchanger transporting the heat energy. (j) Solubility of CO_2 in water as a function of temperature at different partial pressure levels of CO_2 , indicating the increased mass transfer resistance regarding CO_2 at elevated temperatures.^[128] Copyright 2025, Springer Nature.

highlighted the positive effect of membrane hydration on the reaction.^[106] Sargent et al. developed a 3D catalyst: ionomer bulk heterojunction (CIBH) using perfluorinated sulfonic acid (PFSA) ionomers to separate gas, ion, and electron transport pathways. On metal surfaces, gas transport is facilitated by side chains in the hydrophobic domains, enabling extended gas diffusion, while hydrated hydrophilic regions allow for water uptake and ion transport.^[107]

From the perspective of MEA system, simulation-based methods are critical for analyzing mass transport during CO₂R, especially in scaled-up CO₂R electrolyzers. Wu and He et al. developed a mass transport model to calculate the concentrations of CO₂ and H₂ in flow channels and predict CO₂ conversion at different pressures during HCOO⁻ production. Their model provided system-level insights into CO₂R and HER performance.^[108] Lee et al. used a 3D fluid dynamics model to simulate mass transfer enhancements. They introduced unidirectional uniform distribution flow (UDF) channels to design high-performance CO₂ electrolyzers by analyzing convective velocity and flow uniformity.^[109] Seger et al. demonstrated that porous silver filtration membranes serving as GDEs for CO₂-to-CO conversion achieved a CO FE of over 90% at a CO partial current density of ~200 mA cm⁻² at a cell voltage of ~3.3 V. Their experiments revealed that CO₂ crossover reduced the gas flow rate at the cathode outlet, cautioning that using the inlet CO₂ flow rate to calculate the partial current densities and FEs could overestimate electrochemical performance.^[79]

Cathode flooding has emerged as a key challenge for both carbon-based and PTFE-based GDEs, as the CO₂R process critically depends on maintaining a finely tuned three-phase interface with controlled water content.^[108] During the CO₂R process, when H₂O water is used as the primary proton source, the consumption of protons leads to the generation of OH⁻ ions at the cathode surface, raising the local pH. This alkaline environment destabilizes the hydrophobic structure of GDEs, particularly under high current densities where the electrowetting effect is significantly amplified. Carbonate precipitation further compromises the hydrophobicity of GDE, exacerbating mass transport and reducing the overall efficiency of the CO₂R process. The decline in GDE hydrophobicity facilitates water infiltration, accompanied by cations. Recent research by Wessling et al. utilized confocal laser scanning microscopy (CLSM) to investigate how electrowetting dynamics occur.^[109] As shown in Figure 9e-g, they analyzed the GDE pore filling rate along with the related CLSM images and electrolyte contact angles under various conditions. When the potential was set to -1 V, a marked decrease in the contact angle indicated electrolyte penetration into the pores. This electrowetting effect was reversible, as the contact angle recovered once the potential was removed.

As shown in Figure 9d, based on capillary pressure, the pore-size distribution of the catalyst layer, and its wettability, the pores in the GDE can be either flooded, wetted, or dry.^[110] A catalyst layer is considered partially wetted when it contains a combination of flooded and dry pores. Dry pores, lacking an aqueous electrolyte and ionic pathways, become inactive. To minimize CO₂ transport resistance, the electrolyte film in the wetted pores must be thin, yet sufficient thickness is

needed to preserve good ionic conductivity within the catalyst layer. To maintain stable catalytic performance, research often involves adjusting the pore-size distribution or the wettability of the catalyst layer pores to regulate the wetting characteristics. However, the continuous occurrence of cathode flooding results in excessive water covering the catalyst surface, disrupting the initial three-phase interface, leading to severe HER, and adversely affecting product selectivity and device stability.

In standard alkaline or neutral systems, salt formation arises from the interaction of three critical components in CO₂R: CO₂, a proton source (H₂O or HCO₃⁻), and cations that facilitate the reaction (Figure 9j,k).^[111] Although AEMs are mainly intended to block cation transport, some cations can still reach the cathode surface in AEM electrolyzers, often accompanying neutral water molecules. Furthermore, under a strong negative potential at the cathode, electroosmotic flows facilitate cations migration through the AEM. Conversely, in CEM electrolyzers, the positive electric field promotes the movement of cations from the anode to the cathode. As the concentration of carbonate salts rises, saturation is eventually reached, causing salts to precipitate onto the catalyst layer surface. These deposits are usually porous and hygroscopic, enabling electrolyte penetration into the GDE. Over time, excess salt accumulates as efflorescence in the flow-field channels, which can ultimately result in MEA failure.^[112] Seger et al. utilized operando wide-angle X-ray scattering (WAXS) to directly monitor electrolyte infiltration and the onset of salt precipitation (Figure 9f).^[113] Notably, the results reveal that salt precipitation precedes electrolyte penetration into the cathode, as indicated by a shift in X-ray intensity from purple to yellow, corresponding to the presence of the electrolyte and KHCO₃. This finding suggests that salt precipitation is caused by flooding, indicating that flooding and salt precipitation may be independent yet mutually reinforcing processes.^[114,115] Furthermore, the hydrophobic properties of the GDE can be influenced by pressure changes between the two compartments, as well as by defects or cracks within the GDE. According to Kong et al., cracks in the microporous structure of the GDE may mitigate flooding by providing additional pathways for gas transport. At the same time, the fibrous layer of GDEs has been shown to act as a reservoir for water, preventing excessive penetration of water into the catalyst layer.^[116] Despite this, the precise effect of these cracks remains debated, as other studies have indicated that, under certain conditions, these very fissures may exacerbate flooding by facilitating the infiltration of water into the system.^[117]

Efforts to address cathode flooding have centered on improving the hydrophobic properties of the GDE. For instance, Vermaas et al. conducted a comparison of different types of commercially available GDEs and discovered that woven carbon cloth GDEs performed better than nonwoven carbon paper GDEs in terms of CO₂ reduction efficiency.^[118] To further improve water resistance, various hydrophobic additives, such as PTFE, carbon black, and alkyl chains, can be incorporated into the structure.^[99,119] It is important to note that the surface characteristics of the pores, including their wettability, play a role in flood resistance and CO₂ transport than the pore size itself, and this warrants investigation in future studies. Alternatively, the

surface coordination strategy can be employed to enhance the hydrophobicity and performance of the catalyst.^[120–123] However, it should be noted that there is often a compromise between the resistance to flooding and the efficiency of mass transport, with factors such as the thickness and presence of cracks in the GDE structure playing a crucial role in this balance.^[117]

Despite efforts to address the issue of carbonate salt precipitation, a complete elimination of this problem has yet to be achieved. One potential approach to mitigating salt precipitation is to control the type and concentration of cations, keeping them below the threshold for salt crystallization. As an illustration, Liu et al. demonstrated long-term stability by employing a diluted KHCO_3 anolyte (10 mM), maintaining operation for up to 3800 h at 200 mA cm^{-2} and 3 V without encountering flooding or salt formation.^[26] However, it also increases overall cell resistance and voltage due to the lower ionic conductivity of the diluted anolyte. Another tactic involves replacing commonly used cations such as K^+ or Na^+ with Cs^+ , which has higher solubility and is less prone to forming precipitates under similar conditions.^[111] Additionally, dynamic operation protocols, such as periodic electrolyte flushing or potential cycling, have been explored to disrupt the precipitation-dissolution equilibrium and maintain system stability over extended periods.^[12] Beyond this, researchers have investigated alternative strategies such as modifying the AEM to selectively regulate cation transport or substituting cations within the AEM itself, aiming to balance performance and minimize salt-related issues without compromising ionic conductivity. A more recent approach involves the use of pure water as the anolyte, which may offer a promising route toward fundamentally eliminating carbonate salt precipitation.^[91,92]

For MEA electrolyzers to be practically viable, products separation is a key factor. Enhancing CO_2R conversion and selectivity reduces the costs associated with gas product separation in the gas diffusion electrode chamber. However, the collection of liquid products (such as alcohols, formic acid, and acetic acid) is more complex in MEA systems. This complexity arises in part from the absence of a catholyte; liquid products tend to accumulate at the cathode-membrane interface or may transport cross via membrane into anolyte. In addition, liquid product could reduce GDE hydrophobicity and cause membrane swelling to increase its crossover.^[124] For instance, Leonard et al. reported that alcohol concentrations below 30 wt% causes GDE flooding.^[125] The crossover of liquid products to the anode was observed by Luo et al., who found that nearly 90% of the generated acetate ended up in the anolyte. They identified the migration of acetate anions across the AEM as the main cause of this phenomenon, underscoring the vital role of membrane selectivity in optimizing product distribution and sustaining system efficiency.^[126] Moreover, Niu et al. showed that formate ions in the anolyte undergoes oxidation at the anode when using Ni- or Ir-based catalysts.^[127] Currently, laboratory-scale CO_2 electrolysis (CO_2E) technologies have achieved high reaction rates and selectivity at ambient temperatures (20–25 °C). However, significant thermal management challenges arise during scale-up. While high-temperature operation may alleviate salt precipitation and reduce cell voltage, it also imposes new

demands on catalyst stability, membrane durability, and water management. Figure 9i–k summarized the impact of temperature on CO_2R performance, including enhanced conductivity of the electrolyte and membrane, reduced CO_2 solubility, and altered adsorption-desorption and reaction kinetics. Although elevated temperatures may decrease CO_2 solubility, experiments have shown that CO can still be produced efficiently on silver catalysts. While high temperatures help mitigate salt precipitation, they may exacerbate the complexity of water management. The heat distribution within the electrolyzer was quantified using an equivalent circuit model of heat sources and heat dissipation pathways. The heat sources primarily originate from reaction overpotentials and ohmic losses, while heat dissipation relies on the electrolyte, gas flow, and surface cooling. By comparing the advantages and disadvantages of direct cooling and electrolyte loop cooling, noting that industrial cooling water (27–35 °C) requires a temperature difference of ≥ 10 °C with the electrolyte, thereby forcing the electrolyzer to operate at a minimum temperature of 40 °C. In addition, the solubility of CO_2 decreases by a factor of 2.5 with increasing temperature, which may limit mass transfer; however, the solubility of KHCO_3 increases from 3.63 to 6.73 mol/L, alleviating salt blockage. Figure 9i–k shows that the membrane conductivity is enhanced at high temperatures (OH^- conductivity increases from 72.4 to 127.7 mS/cm), providing a basis for optimizing working temperature window (e.g., 50–60 °C).^[128]

5. Ion Exchange Membranes

Ion exchange membranes (IEMs) are vital components in CO_2 electrolyzers, serving to separate the reaction environments of the two half-cells while significantly influencing the overall performance of CO_2R . By partitioning the anode and cathode compartments, IEMs regulate the selective transport of reactive ions, minimize product crossover, and mitigate the re-oxidation of reaction products. Additionally, they provide mechanical stability, ensuring the system withstands pressure differences between compartments. An ideal ion exchange membrane should possess superior ionic transport capabilities, exceptional chemical stability, and sufficient mechanical durability to support continuous operation within MEAs for thousands of hours. Furthermore, IEM determines the full-cell EE.

IEMs applied for electrochemical CO_2R can be divided into three main categories (Figure 10). AEMs can selectively pass anions (e.g., HCO_3^- , and OH^-), CEMs can selectively pass cations (e.g., K^+ , and H^+), and the bipolar membrane (BPM), which is a combination of PEM and AEM, can pass anions and cations on different ends. The selection of the membrane depends on the required operational conditions.

Since AEM allows for the transport of anions and restricts the migration of H^+ ions toward the cathode, it suppresses the competing HER. AEMs are typically paired with alkaline or neutral electrolytes,^[130] where the transport of only OH^- ions within the electrolyte membrane helps sustain a stable reduction reaction environment at the cathode and ensures high ionic

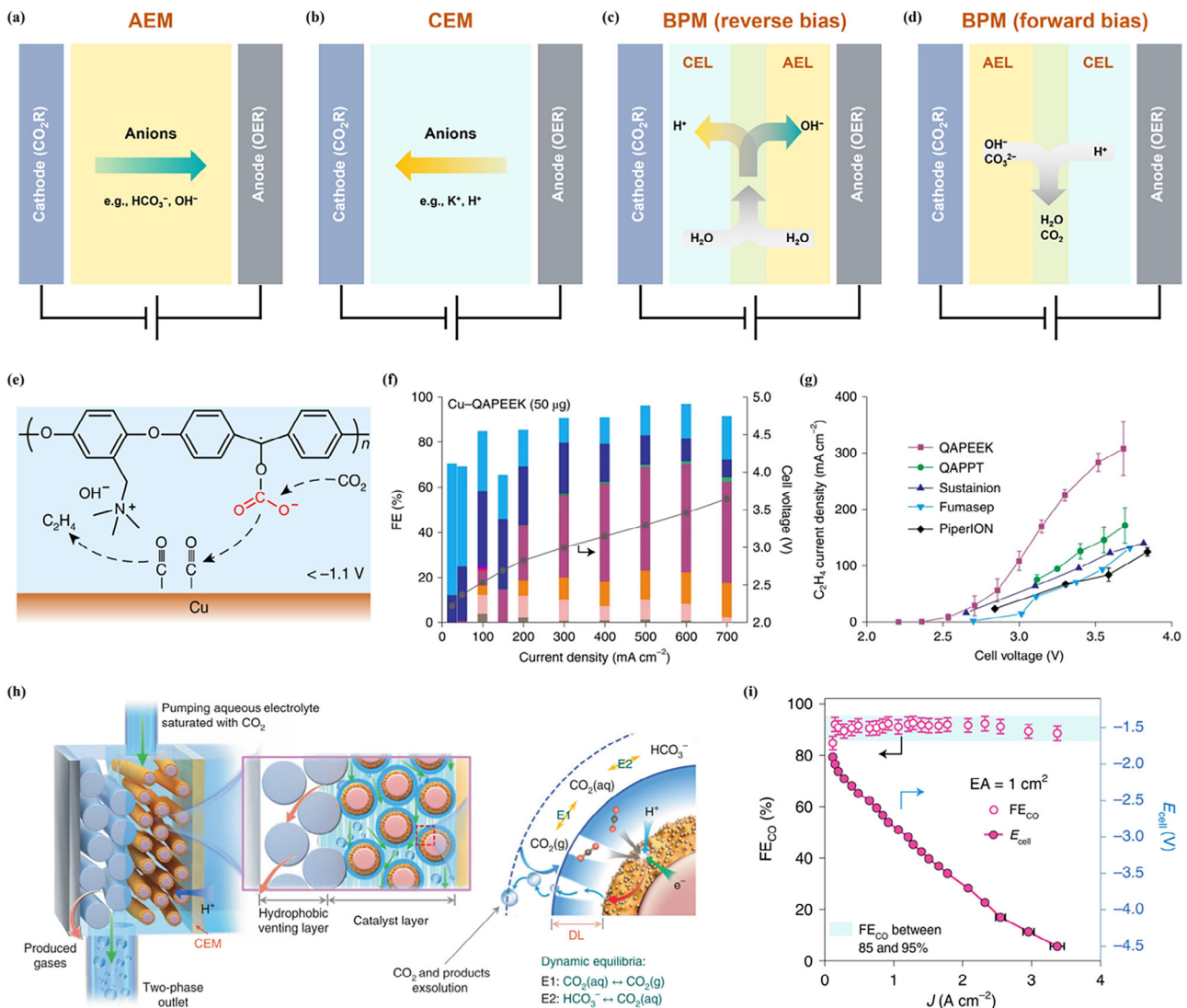


Figure 10. Graphical illustration of different cell configurations: (a) Anion exchange membrane (AEM), (b) Cation exchange membrane (CEM), (c) Bipolar membrane (BPM) in reverse bias, and (d) BPM in forward bias. (e) schematic illustration of the QAPEEK promoted CO₂RR on Cu. (f) C₂H₄ partial current densities of the Cu–QAPEEK GDEs. (g) C₂H₄ partial current densities of the Cu GDEs impregnated with different ionomers.^[91] Copyright 2022, Springer Nature. (h) Illustration of the FTDT cell for pumping CO₂-saturated catholyte throughout a porous electrode with CO₂ exsolution from the dynamic equilibria E1 and E2. CEM, cation exchange membrane; (i) FE_{CO} and cell voltage versus current density in a FTDT cells of 1 cm².^[29] Copyright 2022, Springer Nature.

conductivity. AEM shows no problem when used in CO electroreduction. Nonetheless in CO₂R, OH⁻ ions interact with CO₂ to generate HCO₃⁻/CO₃²⁻ species, leading to salt precipitation at the cathode and anion crossover to the anode.^[131] The CO₂ utilization efficiency is greatly reduced.

Recent advancements have brought novel membrane materials and designs. For instance, thinner membranes (around 20 µm) with reduced water uptake can effectively limit water-related issues and enhance CO₂R efficiency.^[115] New membrane materials, such as quaternary ammonium poly(*N*-methyl-piperidine-co-*p*-terphenyl) (QAPPT),^[132] PiperION,^[133] and Aemion,^[134] offer superior ion conductivity and chemical stability. These address issues like ion crossover and water management that are present in traditional anion exchange membranes. Notably, the QAPPT membrane allows the use of

pure water as anolyte. This to some extent prevents cation crossover and carbonate precipitation,^[132] while Aemion shows superior resistance to ethanol, enabling high-concentration ethanol production at the cathode.^[135] In addition, to address product crossover, strategies like surface modification of membranes with materials such as silica nanoparticles or carbon nanotubes have also been explored. These modifications can reduce the permeation of small molecules like methanol but may come at the cost of diminished ion conductivity. Despite these efforts, there remains substantial potential for further innovation in membrane design to balance conductivity, selectivity, water uptake, mechanical strength, and chemical stability.

CEMs in MEAs is used for acidic CO₂R. At high current densities, rapid proton consumption near the catalyst surface

may lead to the formation of a mildly alkaline environment, in principle, the (bi)carbonates formed in this process are converted back to CO_2 by protons from the acidic bulk electrolyte. In addition, the electroosmotic flow toward the cathode suppresses product crossover to the anode. However, during long-term operation, experiments found that cations can still lead to salt precipitation at the cathode and a decline in anodic OER performance. Using pure water or dilute acids as electrolytes, without any cations, is studied.^[136]

BPM is composed of an anion exchange layer (AEL) and a cation exchange layer (CEL) pressed together, with a catalytic interface situated between the two layers. In CO_2R , BPM can be placed in two configurations: reverse bias and forward bias (Figure 10a–d).^[137] Berlinguette et al. reported high stability CO production in a BPM-based CO_2 electrolyzer at a current density of 100 mA cm^{-2} and a cell voltage of 3.4 V for 24 h with an FE of about 65%, and 50% CO FE at 200 mA cm^{-2} .^[138] Further improvements have been proposed, such as integrating a solid-supported aqueous layer between the CO_2R catalyst and the BPM to enhance system performance.^[139] However, Vermaas et al. pointed out that the energy required to drive water dissociation in the BPM is influenced by the pH difference between the anode and cathode. When the pH difference is small, the energy consumption increases, reducing the overall EE.^[140] Zhuang et al. used bifunctional ionomers as polymer electrolytes that are not only ionically conductive but can also activate CO_2 at the catalyst/electrolyte interface and favour ethylene synthesis (Figure 10e–g). Chen et al. explicitly elucidated the impact of mass transfer and achieved ampere-level CO_2 electroreduction to CO performance by optimizing mesoscale mass transfer (Figure 10h,i).

6. System-Level Energy Considerations and Device Engineering

The energy efficiency of electrocatalysis is primarily determined by the electrode potential and product selectivity. However, the complex kinetics at the catalyst interface, the reaction energy at active sites, and the environment around the triple-phase interface limit electrode potential and selectivity. To address these issues, it is essential to clarify the energy distribution during the reaction and adopt effective methods to enhance energy and mass transfer. Electrode potential losses mainly consist of thermodynamic, kinetic (overpotential), transport (ohmic), and concentration polarization losses. These impact the EE and FE of the electrolyzer, making the optimization of electrode potential crucial for improving system performance. Weber and Bell et al. analyzed the Cu-based membrane electrode potential distribution using multiscale simulations and proposed optimizing the catalyst layer and membrane thickness and ionic conductivity to reduce electrode potential (Figure 11a).^[106,141]

In addition to direct electrolysis of CO_2 , Sargent et al. proposed a tandem reactor strategy to address these challenges. They propose to split the CO_2 electroreduction into two steps: first, CO_2 is reduced to CO in a solid oxide electrolysis cell (SOEC); subsequently, the CO is converted into C_{2+} products in

a MEA electrolyzer. This integrated SOEC–MEA tandem approach enabled efficient CO_2 -to- C_2H_4 conversion, achieving a C_2H_4 FE of 65% at 150 mA cm^{-2} over 110 h of continuous operation. Compared to the direct route, this strategy eliminates CO_2 loss from carbonate formation and reduces energy intensity by approximately 48% (Figures 11c and 10d).^[142] However, the operation of SOECs requires high temperature, thus demanding additional energy input, and the high-temperature CO produced in the first step can not benefit the second step low-temperature CO electrolysis.^[143]

For low-temperature CO electrolysis, Zhong group constructed a quantitative reaction-transport model to analyze the root causes of poor performance in CO reduction (COR), proposing two key descriptors: $(i_0S^*/\rho_{\text{iq}})^{-1/2}$ and $1 - \exp(-b/S^*)$ (Figure 11b). These link the volumetric exchange current density (i_0S^*), volumetric resistivity (ρ_{iq}), and structure-induced intermediate surface retention (proportional to the specific surface area S^*) as critical factors for controlling the energy and selectivity of COR-to- C_2H_4 . This approach reduced the reaction cell potential to 1.87 V, achieving over 40% EE for C_2H_4 and over 50% for multi-carbon products.^[144]

Scaling up CO_2 electrolysis through MEA stacking is crucial for the practical deployment of electrochemical CO_2 conversion technologies. Unlike single-cell devices, MEA stacks integrate multiple reaction units into a compact, modular configuration. This allows for higher current throughput and increased product yields. This scaling-up approach boosts overall system productivity without reducing EE and facilitates seamless integration with renewable energy sources. As shown in Figure 11e, She et al. designed a six-cell MEA stack based on a pure H_2O -fed APMA-MEA configuration for CO_2 reduction. Operating under a total current of 10 A, the stack, equipped with six SS-Cu GDEs, achieved a FE of approximately 50% for C_2H_4 (Figure 11f). The CO_2 -to- C_2H_4 conversion efficiency in this alkali-cation-free, six-cell APMA-MEA stack reached up to ~39%.^[92] This demonstration of scaled-up operation and long-term stability highlights the promise of APMA-MEA-based systems in advancing electrochemical CO_2R toward industrial-scale ethylene production.

7. Conclusion and Perspective

In this review, we summarize key factors determining the performance of MEA-based electrochemical CO_2 reduction (CO_2R) from the perspectives of reaction kinetics, mass transport, and device-level optimization. We elucidate how catalyst composition and structure, interfacial environment, membrane properties, and device parameters impact selectivity, activity, energy efficiency, and stability. Achieving high selectivity toward a single product demands in-depth understanding of reaction pathways and kinetics, where computational modeling and in situ materials and spectroscopy characterization—correlated with performance under operating conditions—provide insights into the electrochemical process and catalyst evolution during CO_2R reaction. Based on these insights, the design of catalysts tailored to practical environments is key to enhancing selectivity.

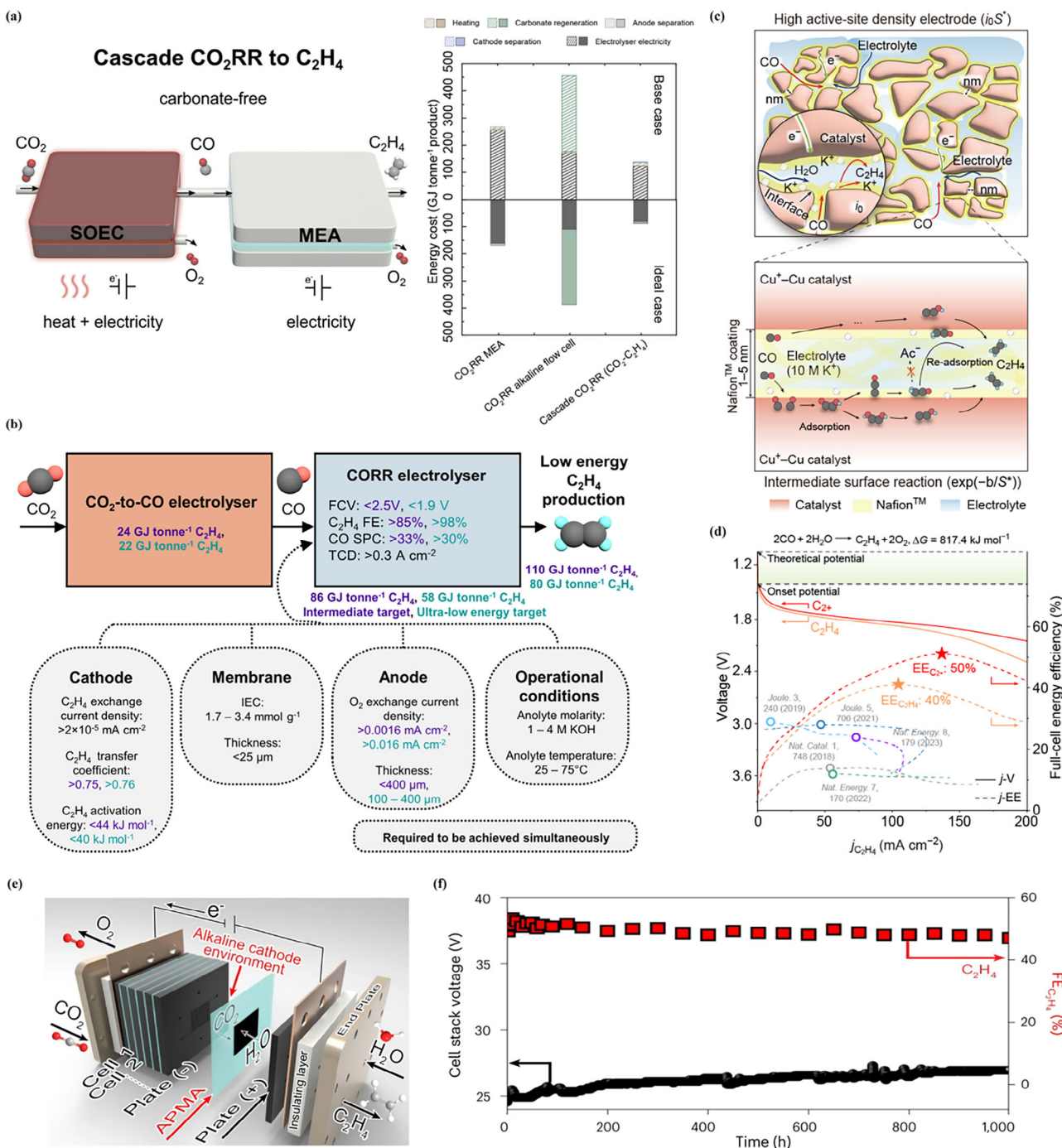


Figure 11. (a) (Left) A cascade approach—coupling a solid-oxide CO₂-to-CO electrolyser (SOEC) with a CO-to-C₂H₄ MEA—would eliminate CO₂ loss to carbonate. (Right) Comparison of energy consumption for C₂H₄ production in various systems.^[142] Copyright 2021, Cell Press. (b) Schematic illustration of pathways toward low-energy-intensity ethylene electroproduction via a cascade system, highlighting the recommended performance metrics for the CO reduction reaction MEA electrolyzer.^[143] Copyright 2024, Cell Press. (c) Schematic illustration of the high active-site density nanonetwork electrode model and the dynamic intermediate surface reaction of the C₂H₄ formation pathway. (d) Summary of the reported EEs for the CO-to-C₂H₄ electroreduction and their achieved EEs and *j*-V performance.^[144] Copyright 2025, Wiley-VCH. (e) A schematic of the APMA-MEA cell stack containing six APMA-MEA cells for the electrocatalytic CO₂R reaction. (f) The system stability performance of electrocatalytic CO₂R to C₂H₄ on SS-Cu in a pure-H₂O-fed APMA-MEA stack (as shown in (e)) at a constant current of 10 A. Each cathode electrode area was 30 cm², and the reaction temperature was 60 °C.^[92] Copyright 2024, Springer Nature.

Attaining high activity requires not only the development of active catalysts but also the enhancement of mesoscale mass and charge transport, which are often dictated as local environment optimization. Advances in artificial intelligence (AI)-

guided identification of key descriptors and new electrochemical mechanisms accelerate the local environment optimization. Stability is influenced by many factors including materials, local electrolyte environment, and gas/liquid transport at the inter-

faces. Overcoming these challenges is vital for continued stability enhancement. Energy efficiency spans multi-scale. Understanding of physicochemical significance of each parameter and their interactions are vital for optimization. We envision that integrated progress—from kinetic insights to mesoscale transport and device-level optimization—will propel MEA development and scale up. Looking ahead, enhancing tolerance to dilute CO₂ streams and complex industrial gases will translate MEA-based CO₂R technology from fundamental research to practical technologies for sustainable energy conversion and chemical production.

Acknowledgments

This work was financially supported by the National Natural Science Foundation of China (grant number 22272078), Frontiers Science Center for Critical Earth Material Cycling, and National University of Singapore – Nanjing University Research Collaboration Fund.

Conflict of Interests

The authors declare no conflict of interest.

Keywords: CO₂ reduction • Electrocatalyst • Electrochemical reaction kinetics • Mass and charge transport • Membrane electrode assembly

- [1] International Energy Agency, can be found under <https://www.iea.org/reports/global-energy-review-co2-emissions-in-2021-2>, 2022 (accessed: April 25, 2025).
- [2] I. Gençü, S. Whitley, M. Trilling, L. van der Burg, M. McLynn, L. Worrall, *Clim. Policy* **2020**, *20*, 1010–1023.
- [3] J.-W. DuanMu, F.-Y. Gao, M.-R. Gao, *Sci. China Mater.* **2024**, *67*, 1721–1739.
- [4] T. Cheng, H. Xiao, W. A. Goddard III, *J. Am. Chem. Soc.* **2016**, *138*, 13802–13805.
- [5] N. Zhu, X. Zhang, N. Chen, J. Zhu, X. Zheng, Z. Chen, T. Sheng, Z. Wu, Y. Xiong, *J. Am. Chem. Soc.* **2023**, *145*, 24852–24861.
- [6] H. Jiang, Z. Fan, M. Zhang, S. Guo, L. Li, X. Yu, Z. Liu, W. Wang, H. Dong, M. Zhong, *ChemElectroChem* **2023**, *10*, e202201164.
- [7] B. Zhang, Z. Guo, Z. Zuo, W. Pan, J. Zhang, *Appl. Catal. B* **2018**, *239*, 441–449.
- [8] Z. Li, A. Cao, Q. Zheng, Y. Fu, T. Wang, K. T. Arul, J. L. Chen, B. Yang, N. M. Adli, L. Lei, C. L. Dong, J. Xiao, G. Wu, Y. Hou, *Adv. Mater.* **2021**, *33*, e2005113.
- [9] M. Wang, H. Chen, M. Wang, J. Wang, Y. Tu, W. Li, S. Zhou, L. Kong, G. Liu, L. Jiang, G. Wang, *Angew. Chem., Int. Ed.* **2023**, *62*, e202306456.
- [10] X. Yu, Y. Xu, L. Li, M. Zhang, W. Qin, F. Che, M. Zhong, *Nat. Commun.* **2024**, *15*, 1711.
- [11] T. Zheng, C. Liu, C. Guo, M. Zhang, X. Li, Q. Jiang, W. Xue, H. Li, A. Li, C. W. Pao, J. Xiao, C. Xia, J. Zeng, *Nat. Nanotechnol.* **2021**, *16*, 1386–1393.
- [12] L. Li, A. Ozden, S. Guo, A. d. A. F. P. Garci, C. Wang, M. Zhang, J. Zhang, H. Jiang, W. Wang, H. Dong, D. Sinton, E. H. Sargent, M. Zhong, *Nat. Commun.* **2021**, *12*, 5223.
- [13] N. Ye, K. Wang, Y. Tan, Z. Qian, H. Guo, C. Shang, Z. Lin, Q. Huang, Y. Liu, L. Li, Y. Gu, Y. Han, C. Zhou, M. Luo, S. Guo, *Nat. Synth.* **2025**, <https://doi.org/10.1038/s44160-025-00769-9>.
- [14] W. Fang, W. Guo, R. Lu, Y. Yan, X. Liu, D. Wu, F. M. Li, Y. Zhou, C. He, C. Xia, H. Niu, S. Wang, Y. Liu, Y. Mao, C. Zhang, B. You, Y. Pang, L. Duan, X. Yang, F. Song, T. Zhai, G. Wang, X. Guo, B. Tan, T. Yao, Z. Wang, B. Y. Xia, *Nature* **2024**, *626*, 86–91.
- [15] C. Xia, P. Zhu, Q. Jiang, Y. Pan, W. Liang, E. Stavitski, H. N. Alshareef, H. Wang, *Nat. Energy* **2019**, *4*, 776–785.
- [16] L. Fan, C. Xia, P. Zhu, Y. Lu, H. Wang, *Nat. Commun.* **2020**, *11*, 3633.
- [17] M. Kunitski, N. Eicke, P. Huber, J. Kohler, S. Zeller, J. Voigtsberger, N. Schlott, K. Henrichs, H. Sann, F. Trinter, L. P. H. Schmidt, A. Kalinin, M. S. Schoffler, T. Jahnke, M. Lein, R. Dorner, *Nat. Commun.* **2019**, *10*, 1.
- [18] F. P. Garcia de Arquer, O. S. Bushuyev, P. De Luna, C. T. Dinh, A. Seifitokaldani, M. I. Saidaminov, C. S. Tan, L. N. Quan, A. Proppe, M. G. Kibria, S. O. Kelley, D. Sinton, E. H. Sargent, *Adv. Mater.* **2018**, *30*, e1802858.
- [19] X. Zheng, P. De Luna, F. P. García de Arquer, B. Zhang, N. Becknell, M. B. Ross, Y. Li, M. N. Banis, Y. Li, M. Liu, O. Voznyy, C. T. Dinh, T. Zhuang, P. Stadler, Y. Cui, X. Du, P. Yang, E. H. Sargent, *Joule* **2017**, *1*, 794–805.
- [20] Z. Li, Z. Zhu, J. Wang, Y. Lin, W. Li, Y. Chen, X. Niu, X. Qi, J. Wang, J. S. Chen, R. Wu, *Adv. Funct. Mater.* **2024**, *34*, 2410552.
- [21] H. Jiang, L. Wang, C. Wang, Y. Xie, C. Shi, Y. Xiao, Y. Liu, W. Ding, M. Zhong, *Nano Lett.* **2025**, *25*, 3579–3587.
- [22] Y. Chen, C. W. Li, M. W. Kanan, *J. Am. Chem. Soc.* **2012**, *134*, 19969–19972.
- [23] X. Shen, X. Liu, S. Wang, T. Chen, W. Zhang, L. Cao, T. Ding, Y. Lin, D. Liu, L. Wang, W. Zhang, T. Yao, *Nano Lett.* **2021**, *21*, 686–692.
- [24] Q. Lu, J. Rosen, Y. Zhou, G. S. Hutchings, Y. C. Kimmel, J. G. Chen, F. Jiao, *Nat. Commun.* **2014**, *5*, 3242.
- [25] S. Wang, Z. Qian, Q. Huang, Y. Tan, F. Lv, L. Zeng, C. Shang, K. Wang, G. Wang, Y. Mao, Y. Wang, Q. Zhang, L. Gu, S. Guo, *Adv. Energy Mater.* **2022**, *12*, 2201278.
- [26] Z. Liu, H. Yang, R. Kutz, R. I. Masel, *J. Electrochem. Soc.* **2018**, *165*, J3371–J3377.
- [27] B. Pan, J. Fan, J. Zhang, Y. Luo, C. Shen, C. Wang, Y. Wang, Y. Li, *ACS Energy Lett.* **2022**, *7*, 4224–4231.
- [28] O. S. Bushuyev, P. De Luna, C. T. Dinh, L. Tao, G. Saur, J. van de Lagemaat, S. O. Kelley, E. H. Sargent, *Joule* **2018**, *2*, 825–832.
- [29] H. Jiang, L. Wang, H. Kaneko, R. Gu, G. Su, L. Li, J. Zhang, H. Song, F. Zhu, A. Yamaguchi, J. Xu, F. Liu, M. Miyauchi, W. Ding, M. Zhong, *Nat. Catal.* **2023**, *6*, 519–530.
- [30] "DOE Announces Goal to Cut Solar Costs by More than Half by 2030", Department of Energy, can be found under <https://www.energy.gov/articles/doe-announces-goal-cut-solar-costs-more-half-2030>, 2021 (accessed: April 26, 2025).
- [31] S. Nitopi, E. Bertheussen, S. B. Scott, X. Liu, A. K. Engstfeld, S. Horch, B. Seger, I. E. L. Stephens, K. Chan, C. Hahn, J. K. Nørskov, T. F. Jaramillo, I. Chorkendorff, *Chem. Rev.* **2019**, *119*, 7610–7672.
- [32] C.-T. Dinh, T. Burdyny, M. G. Kibria, A. Seifitokaldani, C. M. Gabardo, F. P. García de Arquer, A. Kiani, J. P. Edwards, P. De Luna, O. S. Bushuyev, C. Zou, R. Quintero-Bermudez, Y. Pang, D. Sinton, E. H. Sargent, *Science* **2018**, *360*, 783–787.
- [33] R. Chen, Y. Jiang, Y. Zhu, L. Zhang, Y. Li, C. Li, *Adv. Funct. Mater.* **2024**, *35*.
- [34] M. Zhong, K. Tran, Y. Min, C. Wang, Z. Wang, C.-T. Dinh, P. De Luna, Z. Yu, A. S. Rasouli, P. Brodersen, S. Sun, O. Voznyy, C.-S. Tan, M. Askerka, F. Che, M. Liu, A. Seifitokaldani, Y. Pang, S.-C. Lo, A. Ip, Z. Ulissi, E. H. Sargent, *Nature* **2020**, *581*, 178–183.
- [35] J. Zhang, C. Guo, S. Fang, X. Zhao, L. Li, H. Jiang, Z. Liu, Z. Fan, W. Xu, J. Xiao, M. Zhong, *Nat. Commun.* **2023**, *14*, 1298.
- [36] W. Choi, Y. Chae, E. Liu, D. Kim, W. S. Drisdell, H. S. Oh, J. H. Koh, D. K. Lee, U. Lee, D. H. Won, *Nat. Commun.* **2024**, *15*, 8345.
- [37] Y. Wang, Z. Wang, C.-T. Dinh, J. Li, A. Ozden, M. Golam Kibria, A. Seifitokaldani, C.-S. Tan, C. M. Gabardo, M. Luo, H. Zhou, F. Li, Y. Lum, C. McCallum, Y. Xu, M. Liu, A. Proppe, A. Johnston, P. Todorovic, T.-T. Zhuang, D. Sinton, S. O. Kelley, E. H. Sargent, *Nat. Catal.* **2020**, *3*, 98–106.
- [38] C. Choi, S. Kwon, T. Cheng, M. Xu, P. Tieu, C. Lee, J. Cai, H. M. Lee, X. Pan, X. Duan, W. A. Goddard, Y. Huang, *Nat. Catal.* **2020**, *3*, 804–812.
- [39] M. Favaro, H. Xiao, T. Cheng, W. A. Goddard, J. Yano, E. J. Crumlin, *Proc. Natl. Acad. Sci.* **2017**, *114*, 6706–6711.
- [40] S. Mu, H. Lu, Q. Wu, L. Li, R. Zhao, C. Long, C. Cui, *Nat. Commun.* **2022**, *13*, 3694.
- [41] W. Liu, P. Zhai, A. Li, B. Wei, K. Si, Y. Wei, X. Wang, G. Zhu, Q. Chen, X. Gu, R. Zhang, W. Zhou, Y. Gong, *Nat. Commun.* **2022**, *13*, 1877.
- [42] J. Timoshenko, A. Bergmann, C. Rettenmaier, A. Herzog, R. M. Arán-Ais, H. S. Jeon, F. T. Haase, U. Hejral, P. Grosse, S. Kühl, E. M. Davis, J. Tian, O. Magnussen, B. R. Cuenya, *Nat. Catal.* **2022**, *5*, 259–267.

- [43] W. Ma, S. Xie, T. Liu, Q. Fan, J. Ye, F. Sun, Z. Jiang, Q. Zhang, J. Cheng, Y. Wang, *Nat. Catal.* **2020**, *3*, 478–487.
- [44] S. Ren, X. Cao, Q. Fan, Z. Yang, F. Wang, X. Wang, L. Bai, J. Yang, *Nano-Micro Lett.* **2024**, *16*, 262.
- [45] Y. Jiang, Y. Wang, W. Chen, R. Chen, Y. Li, C. Li, *ACS Catal.* **2024**, *14*, 9870–9876.
- [46] C. Yan, W. Luo, H. Yuan, G. Liu, R. Hao, N. Qin, Z. Wang, K. Liu, Z. Wang, D. Cui, Z. Hu, Y. Lan, Z. Lu, *Appl. Catal. B* **2022**, *308*, 121191.
- [47] F. Li, A. Thevenon, A. Rosas-Hernandez, Z. Wang, Y. Li, C. M. Gabardo, A. Ozden, C. T. Dinh, J. Li, Y. Wang, J. P. Edwards, Y. Xu, C. McCallum, L. Tao, Z. Q. Liang, M. Luo, X. Wang, H. Li, C. P. O'Brien, C. S. Tan, D. H. Nam, R. Quintero-Bermudez, T. T. Zhuang, Y. C. Li, Z. Han, R. D. Britt, D. Sinton, T. Agapie, J. C. Peters, E. H. Sargent, *Nature* **2020**, *577*, 509–513.
- [48] T. T. H. Hoang, S. Ma, J. I. Gold, P. J. A. Kenis, A. A. Gewirth, *ACS Catal.* **2017**, *7*, 3313–3321.
- [49] X. He, L. Lin, X. Li, M. Zhu, Q. Zhang, S. Xie, B. Mei, F. Sun, Z. Jiang, J. Cheng, Y. Wang, *Nat. Commun.* **2024**, *15*, 9923.
- [50] H. Li, P. Wei, T. Liu, M. Li, C. Wang, R. Li, J. Ye, Z. Y. Zhou, S. G. Sun, Q. Fu, D. Gao, G. Wang, X. Bao, *Nat. Commun.* **2024**, *15*, 4603.
- [51] W. Luc, X. Fu, J. Shi, J.-J. Lv, M. Jouny, B. H. Ko, Y. Xu, Q. Tu, X. Hu, J. Wu, Q. Yue, Y. Liu, F. Jiao, Y. Kang, *Nat. Catal.* **2019**, *2*, 423–430.
- [52] X. Sun, Q. Zhu, X. Kang, H. Liu, Q. Qian, J. Ma, Z. Zhang, G. Yang, B. Han, *Green Chem.* **2017**, *19*, 2086–2091.
- [53] X. F. Qiu, J. R. Huang, C. Yu, Z. H. Zhao, H. L. Zhu, Z. Ke, P. Q. Liao, X. M. Chen, *Angew. Chem., Int. Ed.* **2022**, *61*, e202206470.
- [54] Y. Cai, R. Yang, J. Fu, Z. Li, L. Xie, K. Li, Y.-C. Chang, S. Ding, Z. Lyu, J.-R. Zhang, J.-J. Zhu, Y. Lin, W. Zhu, *Nat. Synth.* **2024**, *3*, 891–902.
- [55] R. Dorakhan, I. Grigioni, B.-H. Lee, P. Ou, J. Abed, C. O'Brien, A. Sedighian Rasouli, M. Plodinec, R. K. Miao, E. Shirzadi, J. Wicks, S. Park, G. Lee, J. Zhang, D. Sinton, E. H. Sargent, *Nat. Synth.* **2023**, *2*, 448–457.
- [56] J. Jin, J. Wicks, Q. Min, J. Li, Y. Hu, J. Ma, Y. Wang, Z. Jiang, Y. Xu, R. Lu, G. Si, P. Papangelakis, M. Shakouri, Q. Xiao, P. Ou, X. Wang, Z. Chen, W. Zhang, K. Yu, J. Song, X. Jiang, P. Qiu, Y. Lou, D. Wu, Y. Mao, A. Ozden, C. Wang, B. Y. Xia, X. Hu, V. P. Dravid, Y. M. Yiu, T. K. Sham, Z. Wang, D. Sinton, L. Mai, E. H. Sargent, Y. Pang, *Nature* **2023**, *617*, 724–729.
- [57] Y. Ji, Z. Chen, R. Wei, C. Yang, Y. Wang, J. Xu, H. Zhang, A. Guan, J. Chen, T.-K. Sham, J. Luo, Y. Yang, X. Xu, G. Zheng, *Nat. Catal.* **2022**, *5*, 251–258.
- [58] X. P. Yang, Z. Z. Wu, Y. C. Li, S. P. Sun, Y. C. Zhang, J. W. Duanmu, P. G. Lu, X. L. Zhang, F. Y. Gao, Y. Yang, Y. H. Wang, P. C. Yu, S. K. Li, M. R. Gao, *Nat. Commun.* **2025**, *16*, 2811.
- [59] T. Zheng, M. Zhang, L. Wu, S. Guo, X. Liu, J. Zhao, W. Xue, J. Li, C. Liu, X. Li, Q. Jiang, J. Bao, J. Zeng, T. Yu, C. Xia, *Nat. Catal.* **2022**, *5*, 388–396.
- [60] Y. Wen, C. Zhan, J. Liu, X. Zhuang, S. Liu, T. Yang, W. Liu, X. Liu, C. W. Kao, Y. C. Huang, T. S. Chan, Z. Hu, D. Su, J. Han, N. Chen, X. Huang, *Nat. Nanotechnol.* **2025**, *20*, 656–663.
- [61] B. S. Crandall, B. H. Ko, S. Overa, L. Cherniack, A. Lee, I. Minnie, F. Jiao, *Nat. Chem. Eng.* **2024**, *1*, 421–429.
- [62] M. N. Latif, W. N. R. Wan Isahak, A. Samsuri, S. Z. Hasan, W. N. Manan, Z. Yaakob, *Catalysts* **2023**, *13*, 1093.
- [63] Z. Liu, L. Song, X. Lv, M. Liu, Q. Wen, L. Qian, H. Wang, M. Wang, Q. Han, G. Zheng, *J. Am. Chem. Soc.* **2024**, *146*, 14260–14266.
- [64] W. Xia, Y. Xie, S. Jia, S. Han, R. Qi, T. Chen, X. Xing, T. Yao, D. Zhou, X. Dong, J. Zhai, J. Li, J. He, D. Jiang, Y. Yamauchi, M. He, H. Wu, B. Han, *J. Am. Chem. Soc.* **2023**, *145*, 17253–17264.
- [65] X. Chen, S. Jia, J. Zhai, J. Jiao, M. Dong, C. Xue, T. Deng, H. Cheng, Z. Xia, C. Chen, X. Xing, J. Zeng, H. Wu, M. He, B. Han, *Nat. Commun.* **2024**, *15*, 7691.
- [66] P. Wang, H. Yang, C. Tang, Y. Wu, Y. Zheng, T. Cheng, K. Davey, X. Huang, S. Z. Qiao, *Nat. Commun.* **2022**, *13*, 3754.
- [67] C. Chen, S. Yu, Y. Yang, S. Louisia, I. Roh, J. Jin, S. Chen, P.-C. Chen, Y. Shan, P. Yang, *Nat. Catal.* **2022**, *5*, 878–887.
- [68] M. Abdinejad, A. Farzi, R. Möller-Gulland, F. Mulder, C. Liu, J. Shao, J. Biemolt, M. Robert, A. Seifitokaldani, T. Burdyny, *Nat. Catal.* **2024**, *7*, 1109–1119.
- [69] J. Ding, H. Bin Yang, X.-L. Ma, S. Liu, W. Liu, Q. Mao, Y. Huang, J. Li, T. Zhang, B. Liu, *Nat. Energy* **2023**, *8*, 1386–1394.
- [70] H.-T. Kim, J. Park, J. Mun, H. Shin, D.-H. Roh, J. Kwon, S. Kim, S.-J. Kim, G. Lee, S. J. Kang, T.-H. Kwon, *ACS Catal.* **2024**, *14*, 10392–10402.
- [71] L. Zhou, Z. Huang, C. Guan, Y. Zhang, S. Bai, M. Kuang, J. Yang, *Adv. Funct. Mater.* **2025**, *35*, 2418727.
- [72] Q. Li, J. Wu, C. Yang, S. Li, C. Long, Z. Zhuang, Q. Li, Z. Guo, X. Huang, Z. Tang, H. Li, D. Wang, Y. Li, *J. Am. Chem. Soc.* **2025**, *147*, 6688–6697.
- [73] P. P. Yang, X. L. Zhang, F. Y. Gao, Y. R. Zheng, Z. Z. Niu, X. Yu, R. Liu, Z. Z. Wu, S. Qin, L. P. Chi, Y. Duan, T. Ma, X. S. Zheng, J. F. Zhu, H. J. Wang, M. R. Gao, S. H. Yu, *J. Am. Chem. Soc.* **2020**, *142*, 6400–6408.
- [74] N. C. Bhoomik, Q. A. Padovan, T. Akter, D. K. Stem, C. J. Barile, *Angew. Chem., Int. Ed.* **2025**, e202423882.
- [75] Y. Chen, X. Wang, X.-Y. Li, R. K. Miao, J. Dong, Z. Zhao, C. Liu, J. E. Huang, J. Wu, S. Chu, W. Ni, Z. Guo, Y. Xu, P. Ou, B. Xu, Y. Hou, D. Sinton, E. H. Sargent, *Nat. Catal.* **2025**, *8*, 239–247.
- [76] Z. Zhang, L. Melo, R. P. Janssonius, F. Habibzadeh, E. R. Grant, C. P. Berlinquette, *ACS Energy Lett.* **2020**, *5*, 3101–3107.
- [77] J. E. Huang, F. Li, A. Ozden, A. Sedighian Rasouli, F. P. García de Arquer, S. Liu, S. Zhang, M. Luo, X. Wang, Y. Lum, Y. Xu, K. Bertens, R. K. Miao, C.-T. Dinh, D. Sinton, E. H. Sargent, *Science* **2021**, *372*, 1074–1078.
- [78] J. Li, D. Wu, A. S. Malkani, X. Chang, M. J. Cheng, B. Xu, Q. Lu, *Angew. Chem., Int. Ed.* **2020**, *59*, 4464–4469.
- [79] G. O. Larrazabal, P. Strom-Hansen, J. P. Heli, K. Zeiter, K. T. Therkildsen, I. Chorkendorff, B. Seger, *ACS Appl. Mater. Interfaces* **2019**, *11*, 41281–41288.
- [80] Z. Zhang, Q. Lu, J. Sun, G. Li, W. Wu, Z. Xu, L. Xu, Y. Wang, *Chem. Sci.* **2024**, *15*, 2786–2791.
- [81] K. D. Yang, W. R. Ko, J. H. Lee, S. J. Kim, H. Lee, M. H. Lee, K. T. Nam, *Angew. Chem., Int. Ed.* **2017**, *56*, 796–800.
- [82] L. Li, Z. Liu, X. Yu, M. Zhong, *Angew. Chem., Int. Ed.* **2023**, *62*, e202300226.
- [83] Z. Liu, T. Yan, H. Shi, H. Pan, Y. Cheng, P. Kang, *ACS Appl. Mater. Interfaces* **2022**, *14*, 7900–7908.
- [84] M. Moradzaman, G. Mul, *J. Phys. Chem. C* **2021**, *125*, 6546–6554.
- [85] A. Murata, Y. Hori, *Bull. Chem. Soc. Jpn.* **1991**, *64*, 123–127.
- [86] J. Gu, S. Liu, W. Ni, W. Ren, S. Haussener, X. Hu, *Nat. Catal.* **2022**, *5*, 268–276.
- [87] S. Ringe, E. L. Clark, J. Resasco, A. Walton, B. Seger, A. T. Bell, K. Chan, *Energy Environ. Sci.* **2019**, *12*, 3001–3014.
- [88] M. C. O. Monteiro, F. Dattila, N. Lopez, M. T. M. Koper, *J. Am. Chem. Soc.* **2022**, *144*, 1589–1602.
- [89] M. R. Singh, Y. Kwon, Y. Lum, J. W. Ager, 3rd, A. T. Bell, *J. Am. Chem. Soc.* **2016**, *138*, 13006–13012.
- [90] M. C. O. Monteiro, F. Dattila, B. Hagedoorn, R. García-Muelas, N. López, M. T. M. Koper, *Nat. Catal.* **2021**, *4*, 654–662.
- [91] W. Li, Z. Yin, Z. Gao, G. Wang, Z. Li, F. Wei, X. Wei, H. Peng, X. Hu, L. Xiao, J. Lu, L. Zhuang, *Nat. Energy* **2022**, *7*, 835–843.
- [92] X. She, L. Zhai, Y. Wang, P. Xiong, M. M.-J. Li, T.-S. Wu, M. C. Wong, X. Guo, Z. Xu, H. Li, H. Xu, Y. Zhu, S. C. E. Tsang, S. P. Lau, *Nat. Energy* **2024**, *9*, 81–91.
- [93] D. Chen, Y. Wei, Z. Sun, X. Zhao, X. Tang, X. Zhu, G. Li, L. Yao, S. Chen, R. Lin, J. Wang, Q. Li, X. Fan, T. Qiu, Q. Hao, *Small* **2025**, e2409569.
- [94] Y. Hori, A. Murata, R. Takahashi, *J. Chem. Soc., Faraday Trans. 1* **1989**, *85*, 2309–2326.
- [95] J. M. Yoo, J. Ingenmey, M. Salanne, M. R. Lukatskaya, *J. Am. Chem. Soc.* **2024**, *146*, 31768–31777.
- [96] S. Verma, X. Lu, S. Ma, R. I. Masel, P. J. Kenis, *Phys. Chem. Chem. Phys.* **2016**, *18*, 7075–7084.
- [97] T. Burdyny, W. A. Smith, *Energy Environ. Sci.* **2019**, *12*, 1442–1453.
- [98] D. Wakerley, S. Lamaison, J. Wicks, A. Clemens, J. Feaster, D. Corral, S. A. Jaffer, A. Sarkar, M. Fontecave, E. B. Duoss, S. Baker, E. H. Sargent, T. F. Jaramillo, C. Hahn, *Nat. Energy* **2022**, *7*, 130–143.
- [99] Z. Xing, L. Hu, D. S. Ripatti, X. Hu, X. Feng, *Nat. Commun.* **2021**, *12*, 136.
- [100] A. Ozden, F. Li, F. P. García de Arquer, A. Rosas-Hernández, A. Thevenon, Y. Wang, S.-F. Hung, X. Wang, B. Chen, J. Li, J. Wicks, M. Luo, Z. Wang, T. Agapie, J. C. Peters, E. H. Sargent, D. Sinton, *ACS Energy Lett.* **2020**, *5*, 2811–2818.
- [101] A. K. Buckley, T. Cheng, M. H. Oh, G. M. Su, J. Garrison, S. W. Utan, C. Zhu, F. D. Toste, W. A. Goddard, F. M. Toma, *ACS Catal.* **2021**, *11*, 9034–9042.
- [102] D. Wakerley, S. Lamaison, F. Ozanam, N. Menguy, D. Mercier, P. Marcus, M. Fontecave, V. Mougel, *Nat. Mater.* **2019**, *18*, 1222–1227.
- [103] M. L. Aya Buckley, T. Cheng, R. V. Kazantsev, D. M. Larson, W. A. Goddard, F. Dean Toste, F. M. Toma, *J. Am. Chem. Soc.* **2019**, *141*, 7355–7364.
- [104] F. Zeng, H. Deng, M. Zhuansun, W. Teng, Y. Wang, *J. Mater. Chem. A* **2024**, *12*, 20990–20998.

- [105] W. Choi, S. Park, W. Jung, D. H. Won, J. Na, Y. J. Hwang, *ACS Energy Lett.* **2022**, *7*, 939–945.
- [106] L.-C. Weng, A. T. Bell, A. Z. Weber, *Energy Environ. Sci.* **2019**, *12*, 1950–1968.
- [107] F. P. García de Arquer, C.-T. Dinh, A. Ozden, J. Wicks, C. McCallum, A. R. Kirmani, D.-H. Nam, C. Gabardo, A. Seifitokaldani, X. Wang, Y. C. Li, F. Li, J. Edwards, L. J. Richter, S. J. Thorpe, D. Sinton, E. H. Sargent, *Science* **2020**, *367*, 661–666.
- [108] M. Ramdin, O. A. Moulton, L. J. P. van den Broeke, P. Gonugunta, P. Taheri, T. J. H. Vlugt, *Ind. Eng. Chem. Res.* **2023**, *62*, 6843–6864.
- [109] A. M. Kalde, M. Grosseheide, S. Brosch, S. V. Pape, R. G. Keller, J. Linkhorst, M. Wessling, *Small* **2022**, *18*, e2204012.
- [110] L. C. Weng, A. T. Bell, A. Z. Weber, *Phys. Chem. Chem. Phys.* **2018**, *20*, 16973–16984.
- [111] S. Garg, Q. Xu, A. B. Moss, M. Mirolo, W. Deng, I. Chorkendorff, J. Drnec, B. Seger, *Energy Environ. Sci.* **2023**, *16*, 1631–1643.
- [112] K. Yang, R. Kas, W. A. Smith, T. Burdyny, *ACS Energy Lett.* **2020**, *6*, 33–40.
- [113] A. B. Moss, S. Garg, M. Mirolo, C. A. Giron Rodriguez, R. Ilvonen, I. Chorkendorff, J. Drnec, B. Seger, *Joule* **2023**, *7*, 350–365.
- [114] J. Disch, L. Bohn, S. Koch, M. Schulz, Y. Han, A. Tengattini, L. Helfen, M. Breitwieser, S. Vierrath, *Nat. Commun.* **2022**, *13*, 6099.
- [115] D. A. Salvatore, C. M. Gabardo, A. Reyes, C. P. O'Brien, S. Holdcroft, P. Pintauro, B. Bahar, M. Hickner, C. Bae, D. Sinton, E. H. Sargent, C. P. Berlinguette, *Nat. Energy* **2021**, *6*, 339–348.
- [116] Y. Kong, M. Liu, H. Hu, Y. Hou, S. Vesztergom, M. J. Galvez-Vazquez, I. Zelocualtecatl Montiel, V. Kolivoska, P. Broekmann, *Small Methods* **2022**, *6*, e2200369.
- [117] L. M. Baumgartner, C. I. Koopman, A. Forner-Cuenca, D. A. Vermaas, *ACS Sustainable Chem. Eng.* **2022**, *10*, 4683–4693.
- [118] L. M. Baumgartner, C. I. Koopman, A. Forner-Cuenca, D. A. Vermaas, *ACS Appl. Energy Mater.* **2022**, *5*, 15125–15135.
- [119] Y. Wu, L. Charlesworth, I. Maglaya, M. N. Idros, M. Li, T. Burdyny, G. Wang, T. E. Rufford, *ACS Energy Lett.* **2022**, *7*, 2884–2892.
- [120] M. Fang, M. Wang, Z. Wang, Z. Zhang, H. Zhou, L. Dai, Y. Zhu, L. Jiang, *J. Am. Chem. Soc.* **2023**, *145*, 11323–11332.
- [121] Y. Lin, T. Wang, L. Zhang, G. Zhang, L. Li, Q. Chang, Z. Pang, H. Gao, K. Huang, P. Zhang, Z. J. Zhao, C. Pei, J. Gong, *Nat. Commun.* **2023**, *14*, 3575.
- [122] Q. Chang, G. Zhang, Y. Wang, Y. Lin, H. Gao, L. Guo, P. Zhang, C. Pei, T. Wang, J. Gong, *Adv. Funct. Mater.* **2025**, *35*, 2425601.
- [123] W. Li, H. Jiang, X. Zhang, B. Lei, L. Li, H. Zhou, M. Zhong, *J. Am. Chem. Soc.* **2024**, *146*, 21968–21976.
- [124] H. Rabiee, L. Ge, X. Zhang, S. Hu, M. Li, Z. Yuan, *Energy Environ. Sci.* **2021**, *14*, 1959–2008.
- [125] M. E. Leonard, M. J. Orella, N. Aiello, Y. Román-Leshkov, A. Forner-Cuenca, F. R. Brushett, *J. Electrochem. Soc.* **2020**, *167*, 124521.
- [126] M. Luo, A. Ozden, Z. Wang, F. Li, J. E. Huang, S. F. Hung, Y. Wang, J. Li, D. H. Nam, Y. C. Li, Y. Xu, R. Lu, S. Zhang, Y. Lum, Y. Ren, L. Fan, F. Wang, H. H. Li, D. Appadoo, C. T. Dinh, Y. Liu, B. Chen, J. Wicks, H. Chen, D. Sinton, E. H. Sargent, *Adv. Mater.* **2023**, *35*, e2209567.
- [127] Z.-Z. Niu, L.-P. Chi, R. Liu, Z. Chen, M.-R. Gao, *Energy Environ. Sci.* **2021**, *14*, 4169–4176.
- [128] H. M. Pelzer, N. Kolobov, D. A. Vermaas, T. Burdyny, *Nat. Energy* **2025**, *10*, 549–556.
- [129] G. Wen, B. Ren, X. Wang, D. Luo, H. Dou, Y. Zheng, R. Gao, J. Gostick, A. Yu, Z. Chen, *Nat. Energy* **2022**, *7*, 978–988.
- [130] A. Reyes, R. P. Jansonius, B. A. W. Mowbray, Y. Cao, D. G. Wheeler, J. Chau, D. J. Dvorak, C. P. Berlinguette, *ACS Energy Lett.* **2020**, *5*, 1612–1618.
- [131] Y. Xu, R. K. Miao, J. P. Edwards, S. Liu, C. P. O'Brien, C. M. Gabardo, M. Fan, J. E. Huang, A. Robb, E. H. Sargent, D. Sinton, *Joule* **2022**, *6*, 1333–1343.
- [132] Z. Yin, H. Peng, X. Wei, H. Zhou, J. Gong, M. Huai, L. Xiao, G. Wang, J. Lu, L. Zhuang, *Energy Environ. Sci.* **2019**, *12*, 2455–2462.
- [133] B. Endrődi, E. Kecsenovity, A. Samu, T. Halmágyi, S. Rojas-Carbonell, L. Wang, Y. Yan, C. Janáky, *Energy Environ. Sci.* **2020**, *13*, 4098–4105.
- [134] P. Mardle, A. Gangrade, T. Saatkamp, Z. Jiang, S. Cassegrain, N. Zhao, Z. Shi, S. Holdcroft, *ChemSusChem* **2023**, *16*, e202202376.
- [135] C. M. Gabardo, C. P. O'Brien, J. P. Edwards, C. McCallum, Y. Xu, C.-T. Dinh, J. Li, E. H. Sargent, D. Sinton, *Joule* **2019**, *3*, 2777–2791.
- [136] Z. Zhang, X. Huang, Z. Chen, J. Zhu, B. Endrodi, C. Janaky, D. Deng, *Angew. Chem., Int. Ed.* **2023**, *62*, e202302789.
- [137] M. B. McDonald, S. Ardo, N. S. Lewis, M. S. Freund, *ChemSusChem* **2014**, *7*, 3021–3027.
- [138] D. A. Salvatore, D. M. Weekes, J. He, K. E. Dettelbach, Y. C. Li, T. E. Mallouk, C. P. Berlinguette, *ACS Energy Lett.* **2017**, *3*, 149–154.
- [139] Y. C. Li, G. Lee, T. Yuan, Y. Wang, D.-H. Nam, Z. Wang, F. P. García de Arquer, Y. Lum, C.-T. Dinh, O. Voznyy, E. H. Sargent, *ACS Energy Lett.* **2019**, *4*, 1427–1431.
- [140] D. A. Vermaas, W. A. Smith, *ACS Energy Lett.* **2016**, *1*, 1143–1148.
- [141] L.-C. Weng, A. T. Bell, A. Z. Weber, *Energy Environ. Sci.* **2020**, *13*, 3592–3606.
- [142] A. Ozden, Y. Wang, F. Li, M. Luo, J. Sisler, A. Thevenon, A. Rosas-Hernández, T. Burdyny, Y. Lum, H. Yadegari, T. Agapie, J. C. Peters, E. H. Sargent, D. Sinton, *Joule* **2021**, *5*, 706–719.
- [143] T. Alkayyali, M. Zargartalebi, A. Ozden, F. Arabiarmohammadi, R. Dorakhan, J. P. Edwards, F. Li, A. Shayesteh Zeraati, M. Fan, A. Bazylak, E. H. Sargent, D. Sinton, *Joule* **2024**, *8*, 1478–1500.
- [144] J. Zhang, H. Jiang, X. Zhao, Z. Liu, L. Li, W. Ding, M. Zhong, *Chem. Int. Ed.* **2025**, *64*, e202502690.

Manuscript received: May 5, 2025

Revised manuscript received: June 20, 2025

Version of record online: July 11, 2025